

Examining AGN UV/optical Variability Beyond the Simple Damped Random Walk

WEIXIANG YU ¹, GORDON T. RICHARDS ¹, MICHAEL S. VOGELY ¹, JACKELINE MORENO ¹ AND
MATTHEW J. GRAHAM ²

¹*Department of Physics,
Drexel University, 32 S. 32nd Street,
Philadelphia, PA 19104, USA*

²*Department of Physics, Math, and Astronomy
California Institute of Technology
Pasadena, CA, 91125, USA*

(Received June 30, 2022; Revised; Accepted)

ABSTRACT

We present damped harmonic oscillator (DHO) light-curve modeling for a sample of 12,714 spectroscopically confirmed quasars in the Sloan Digital Sky Survey Stripe 82 region. DHO is a second-order continuous-time autoregressive moving-average (CARMA) process, which can be fully described using four independent parameters: a natural oscillation frequency (ω_0), a damping ratio (ξ), a characteristic perturbation timescale (τ_{perturb}), and an amplitude for the perturbing white noise (σ_ϵ). The asymptotic variability amplitude of a DHO process is quantified by σ_{DHO} —a function of ω_0 , ξ , τ_{perturb} , and σ_ϵ . We find that both τ_{perturb} and σ_ϵ follow different dependencies with rest-frame wavelength (λ_{RF}) on either side of 2500 Å, whereas σ_{DHO} follows a single power-law relation with λ_{RF} . After correcting for wavelength dependence, σ_{DHO} exhibits anti-correlations with both the Eddington ratio and the black hole mass, while τ_{perturb} —with a typical value of days in the rest-frame—shows an anti-correlation with the bolometric luminosity. Modeling AGN variability as a DHO offers more insight into the workings of accretion disks close to the supermassive black holes (SMBHs) at the center of AGN. The newly discovered short-term variability (characterized by τ_{perturb} and σ_ϵ) and its correlation with bolometric luminosity pave the way for new algorithms that will derive fundamental properties (e.g., Eddington ratio) of AGN using photometric data alone.

Keywords: quasars, AGN, supermassive black holes — time series analysis — surveys

1. BACKGROUND & MOTIVATION

The UV/optical luminosity of active galactic nuclei (AGN)¹, or quasars at the bright end, is known to vary at the 10% flux level on average from weeks to years (Vanden Berk et al. 2004; Sesar et al. 2007). The time variability of AGN luminosity has been known for decades (Matthews & Sandage 1963), however, the physical mechanisms driving such variability are still unclear. Nevertheless, the success of reverberation map-

ping (Peterson et al. 2004) has shown that the broad emission lines respond to and lag behind the continuum fluctuations, suggesting an accretion disk origin of the UV/optical continuum variability.

Under the assumption that the optical variability originates from the accretion disk close to the SMBH, various models have been proposed to explain the observed variability. Based on the standard α disk model (Shakura & Sunyaev 1973), some have shown that the observed optical variability could be driven by variations in the mass accretion rate (Pereyra et al. 2006; Li & Cao 2008; Liu et al. 2008). Meanwhile, others suggested that it is also possible for the accretion disk to passively reprocess the radiation from the X-ray corona given the observed short time lags between UV/optical

Corresponding author: Weixiang Yu
wy73@drexel.edu

¹ In this manuscript, we will use AGN and quasar interchangeably without making a distinction based on, e.g., luminosity or radio emission.

continuum light curves (Wanders et al. 1997; Sergeev et al. 2005).

Observationally, significant efforts/progress have also been made to investigate the physical origin(s) of the UV/optical variability by virtue of exploring the correlations of variability signatures with the physical properties of AGN. Notable results include: an anti-correlation of variability amplitude with rest-frame wavelength and an anti-correlation of variability with luminosity and/or Eddington ratio (e.g., Vanden Berk et al. 2004; Wilhite et al. 2007; Bauer et al. 2009; MacLeod et al. 2010; Simm et al. 2016; Caplar et al. 2017). Correlations between variability and black hole mass have also been reported in numerous studies (Wold et al. 2007; Wilhite et al. 2007; Bauer et al. 2009; Kelly et al. 2009; MacLeod et al. 2010; Caplar et al. 2017).

Among the different techniques utilized to characterize AGN variability, Kelly et al. (2009) started a new era of directly modeling (inherently non-periodic) AGN light curves using stochastic diffusion processes, in particular, as a damped random walk (DRW) model. The DRW model features a fixed-slope power spectrum density (PSD) at high frequencies (short timescales) and a flat PSD at timescales longer than a characteristic timescale (τ_{DRW}). Modeling AGN variability as a DRW has provided a lot of insight into how AGN luminosity varies in UV/optical and what might be driving it (MacLeod et al. 2010). However, better sampled light curves from the Kepler Mission (Borucki et al. 2010) cast doubt on the DRW description of AGN variability because of the steeper slopes observed in the PSDs at high frequencies (Mushotzky et al. 2011); investigations carried out by other groups also arrived at similar conclusions (Kasliwal et al. 2015; Simm et al. 2016; Smith et al. 2018). This discrepancy motivates the search for new models (and methods) to analyze AGN light curves. Given that the DRW model is the simplest case of a more general class of stochastic diffusion processes, namely the continuous-time autoregressive moving-average processes (CARMA; Brockwell 2001; Roux 2002), Kelly et al. (2014) set up a more flexible framework to model astronomical time series as CARMA processes, where the PSDs of higher-order CARMA processes can take more flexible shapes, for example, a wide range of PSD slopes can be achieved at high frequencies. Later, Kasliwal et al. (2017) demonstrated that the CARMA(2,1) model is a better fit than all other models of CARMA for a well-monitored object Zw229-15. Inspired by the aforementioned discrepancy and the pilot investigations carried out by Kelly et al. (2014) and Kasliwal et al. (2017), Moreno et al. (2019, hereafter M19) conducted an in-depth exploration of the CARMA(2,1) model, oth-

erwise known as the (perturbation-driven) damped harmonic oscillator (DHO) model, and established guidelines for modeling AGN light curves as DHOs.

Here, we build upon the work performed by Kelly et al. (2014), Kasliwal et al. (2017), and Moreno et al. (2019) to model a large statistical sample of AGN as DHOs, examine the variability signatures extracted by the DHO model, and explore the potential correlations between DHO parameters and the physical properties of AGN. We acknowledge that the DHO model (alike the DRW model) is a statistical model rather than a physical model; however, stochastic diffusion processes such as CARMA are a natural choice for parameterizing AGN light curves, and it can reveal interesting variability features embedded in the light curves that could not be unfolded otherwise (see Vio & Andreani (2018) for a discussion about the limitations of CARMA modeling).

In Section 2, we introduce the data set utilized in this work and outline our initial light curve construction procedures. In Section 3, we provide an overview of the DHO model, its key features, and how to use Gaussian process (GP) to extract DHO parameters from light curves. In Section 4, we present the results of fitting DHO to our quasar light curves, layout and test our bad-fit identification algorithm, and explore the effects of light-curve sampling and photometric accuracy on the best-fit DHO parameters. In Section 5, we describe the observed correlations of DHO features with the physical properties of the quasars in our sample, and discuss the associated implications in Section 6. Finally, we summarize our results and provide an outlook for future work in direct modeling of AGN light curves using stochastic diffusion processes in Section 7.

2. THE DATA SET

We compiled a sample of 12,714 spectroscopically confirmed quasars discovered in the Sloan Digital Sky Survey (SDSS) Stripe 82 region (York et al. 2000; Annis et al. 2014), a 120° long and 2.5° wide stripe centered along the celestial equator, from the quasar catalog of SDSS Data Release 16 (DR16Q; Lyke et al. 2020). We refer to this initial sample of quasars as the **main sample**; quasars in this main sample either have their fundamental physical properties (e.g., black hole mass) estimated by Shen et al. (2011) or C IV emission line properties (i.e., equivalent width and blueshift) determined by Rankine et al. (2020). Figure 1 shows the distribution of the main sample quasars in the luminosity and redshift space, where the luminosity (*i*-band absolute magnitude) has been k-corrected to $z = 2$ (Richards et al. 2006).

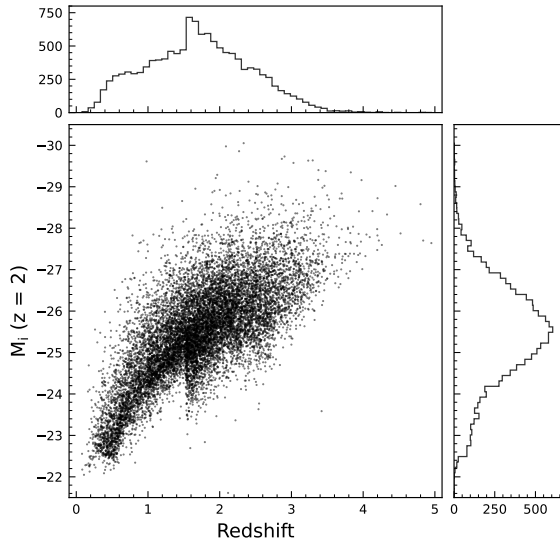


Figure 1. Distribution of the **main sample** quasars in the luminosity (absolute i -band magnitude k -corrected to a redshift of 2) and redshift space. This sample is constructed from the SDSS DR16 quasar catalog—the latest release of SDSS quasar spectra (Lyke et al. 2020); quasars in this sample either have their physical properties estimated by Shen et al. (2011) or CIV emission line properties measured by Rankine et al. (2020).

2.1. The Sloan Digital Sky Survey (2000–2008)

The Sloan Digital Sky Survey obtained images for more than 10,000 deg² of the northern hemisphere down to limiting magnitudes of 22.5, 23.2, 22.6, 21.9, 20.8 at the 50% completeness level in the u, g, r, i, z bands, respectively. The SDSS Stripe 82 (S82) region was observed repeatedly over a 8-year long baseline providing up to 90 single-epoch observations (Frieman et al. 2008; Sako et al. 2008; Abazajian et al. 2009). The SDSS light curves used in this investigation span two phases of the Sloan Digital Sky Survey, namely, the SDSS Legacy Survey (York et al. 2000) and the SDSS-II Supernova Survey (Frieman et al. 2008; Sako et al. 2008), where the latter was performed under less photometric conditions. A so-called “ubercalibration” (Ivezić et al. 2007; Padmanabhan et al. 2008; Bramich et al. 2008), which takes advantage of the overlap between adjacent imaging runs to arrive at a uniform internal calibration, was utilized to achieve a $\sim 1\%$ photometric accuracy in $griz$ and 2% in u for both photometric and less photometric observations. Such a calibration method has become the default since the seventh data release of SDSS (DR7) (Abazajian et al. 2009), from which our light curves were constructed.

2.2. SDSS Light Curves

The SDSS light curves for our quasars were generated by cross matching against the `photoobj` table under the `Stripe82` context on CasJobs² using a 1” matching radius. We imposed an initial quality cut on the matched detections—that is, their photometry must be “clean” and their photometric uncertainties (`psfmagerr`) must be smaller than 1 mag. More on the “clean” flag (and other photometry flags) can be found on SDSS-IV’s website³. The raw light curves are then post-processed following the recipe described below:

1. We first require light curves to have at least 30 epochs.
2. We then remove data points that deviate more than 3σ away from the 3-point running median. This process removes any abnormally large-amplitude variability in the photometry (Graham et al. 2014).
3. Lastly, we remove data points with photometric uncertainties that are more than 5 times larger than the median uncertainty of all photometry in the corresponding light curves.

Note that the post-processing described above is on a per-band basis, that is, failing to have a good light curve in a particular passband does not exclude an object from our sample. The final collection contains $\approx 12,400$ light curves in each u, g, r, i, z band. Those light curves are then fitted with the DHO model. The distributions of four basic statistics of those light curves are shown in Figure 2.

3. METHODOLOGY

We model the time variability of AGN UV/optical luminosity as a DHO, which is formally defined as the solution to the following stochastic differential equation,

$$d^2x + \alpha_1 d^1x + \alpha_2 x = \beta_0 \epsilon(t) + \beta_1 d^1(\epsilon(t)), \quad (1)$$

where $\epsilon(t)$ is Gaussian white noise with an amplitude of unity⁴, α_1 and α_2 are called the autoregressive (AR) coefficients⁵, and β_0 and β_1 are called the moving-average (MA) coefficients. The differentiation is with respect

² <https://skyserver.sdss.org/casjobs/>

³ <https://www.sdss.org/dr16/tutorials/flags/>

⁴ $\epsilon(t) \equiv dW/dt$, W is the Wiener process or referred to as Brownian motion in physics.

⁵ Note that α_0 is defined to be 1 by convention.

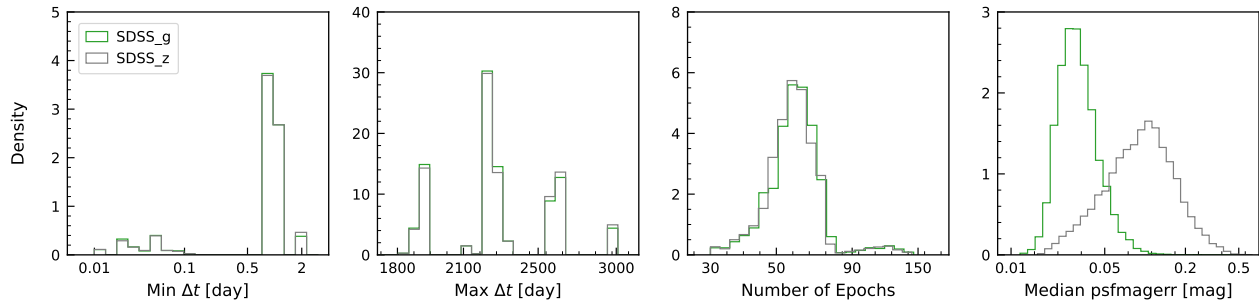


Figure 2. Distribution of SDSS light curve statistics in g and z bands. The statistics shown are (from left to right): minimum time separation between any two observations in a light curve ($\text{Min } \Delta t$); the maximum time separation between any two observations in a light curve ($\text{Max } \Delta t$); number of epochs in a light curve; the median photometric error for observations in a light curve.

to time. Here, x represents the brightness (magnitude⁶ in this work) of the modeled quasars. For a comparison, the stochastic differential equation for the DRW model—a CARMA(1,0) process—has the form⁷,

$$d^1x + \alpha_1x(t) = \beta_0\epsilon(t). \quad (2)$$

3.1. Damped Harmonic Oscillator (DHO)

The utility of modeling quasar light curves as DHOs has been explored and discussed extensively in M19; here we provide a brief introduction to the DHO model under the framework of an impulse-response dynamical system.

In short, we can think of time series (or light curves in this context) following the stochastic differential equation (SDE) shown in Equation 1 as impulse-response dynamical systems. The left-hand-side (LHS) of the SDE describes how the systems respond to impulse perturbations (in the differential form) and the right-hand-side (RHS) describes how the systems are being perturbed/excited. This interpretation connects the DHO process naturally to the classical damped harmonic oscillator, where the classical counterpart has a deterministic driving force on the RHS rather than a stochastic one. Given this analogy, we can rewrite Equation 1 as,

$$d^2x + 2\xi\omega_0d^1x + \omega_0^2x = \sigma_\epsilon\epsilon(t) + \tau_{\text{perturb}}\sigma_\epsilon d^1(\epsilon(t)), \quad (3)$$

where $2\xi\omega_0 = \alpha_1$ and $\omega_0^2 = \alpha_2$. ξ is the damping ratio of the damped oscillator and ω_0 is the natural oscillation

frequency (i.e., when there is no damping). We can classify DHO processes into underdamped ($\xi < 1$) and overdamped ($\xi > 1$) DHOs, each corresponds to a different class of dynamical systems that can be interpreted using the impulse-response framework (Moreno et al. 2019). On the RHS of Equation 3 (compared to Equation 1), we renamed β_0 to σ_ϵ and defined τ_{perturb} as β_1/β_0 . σ_ϵ can be treated as the amplitude of the short-term perturbing white noise ($\epsilon(t)$) with the unit⁸ of magnitude/time^{3/2}. For unit consistency, τ_{perturb} obtains a unit of time and manifests as a characteristic timescale of the perturbation process (Kasliwal et al. 2017; Moreno et al. 2019).

Given Equation 3, we can fully define a DHO process using ξ , ω_0 , σ_ϵ , and τ_{perturb} , where the first two are from the LHS of Equation 3 and the last two are from the RHS of Equation 3. This new set of independent parameters and the four (α_1 , α_2 , β_0 , and β_1) from Equation 1 will be used side by side throughout this manuscript, where the original parameters (from Equation 1) will be used mostly in the technical sections (e.g., Section 3) and the newly defined parameters will be used primarily in the discussion of scientific implications (e.g., Section 5).

Various intrinsic timescales can be extracted from the LHS of Equation 1 (or Equation 3) based on the roots (r_1, r_2) of its characteristic equation,

$$r_1, r_2 = -\frac{\alpha_1}{2} \pm \sqrt{\frac{\alpha_1^2}{4} - \alpha_2} = -\omega_0\xi \pm \omega_0\sqrt{\xi^2 - 1}. \quad (4)$$

When $\xi < 1$ (underdamped DHOs) the two roots are complex conjugates, a decay timescale (τ_{decay}) and a damped oscillation period (T_{dQPO}) can be obtained,

$$\tau_{\text{decay}} = \frac{1}{|\text{Re}(r_1)|} = \frac{1}{\omega_0\xi},$$

⁶ The output of a CARMA process follows a Gaussian distribution, so does the magnitude light curve of a compact accreting object (Uttley & McHardy 2001; Gaskell 2004; MacLeod et al. 2012), thus fitting CARMA models to quasar light curves in magnitude rather than in flux is a logical choice. Meanwhile, for the majority of our sample (dominated by luminous quasars), host galaxy (and other background) star light contamination is negligible (Shen et al. 2011).

⁷ Note that β_0 is equivalent to σ in Kelly et al. (2009, 2014) and $\hat{\sigma}$ in MacLeod et al. (2010).

⁸ The unit of σ_ϵ can be derived by matching the units of the LHS and the RHS of Equation 3 (Kasliwal et al. 2017) given that $\epsilon(t)$ ($\equiv dW/dt$) has the unit of $1/\sqrt{dt}$ (Roux 2002).

$$T_{\text{dQPO}} = \frac{2\pi}{|\text{Im}(r_1)|} = \frac{2\pi}{\omega_0 \sqrt{1 - \xi^2}}. \quad (5)$$

where $2\pi/\omega_0$ is the natural oscillation period (T_{QPO}) associated with ω_0 . T_{dQPO} is effectively the oscillation period in the presence of resistance/damping. For no resistance/damping ($\xi \approx 0$), T_{dQPO} and T_{QPO} become equivalent.

When $\xi > 1$ (overdamped DHOs), both roots are real leaving us a rising timescale (τ_{rise}) and a decay timescale (τ_{decay}),

$$\tau_{\text{rise}} = \left| \frac{1}{\min(r_1, r_2)} \right|, \quad \tau_{\text{decay}} = \left| \frac{1}{\max(r_1, r_2)} \right|. \quad (6)$$

These four timescales (two for each class: underdamped and overdamped) derived from the LHS of Equation 3 set the foundation for describing the response of the modeled dynamical system to a delta function impulse perturbation, whereas τ_{perturb} from the RHS of Equation 3 characterizes how the dynamical system is being driven/excited. In Figure 3, the bottom left panel provides the driving component (RHS of Equation 3) power spectrum densities for three example DHO processes⁹, the bottom middle panel shows the impulse-response functions (LHS of Equation 3), and the bottom right panel plots the resulting time series (light curves).

On top of the intrinsic timescales, M19 also defines a decorrelation timescale, which characterizes the timescale at which the system becomes de-correlated from an earlier excitation (forgets about its past self),

$$\begin{aligned} \text{Underdamped: } \tau_{\text{decorr}} &\approx \frac{\pi}{2} T_{\text{QPO}}, \\ \text{Overdamped: } \tau_{\text{decorr}} &\approx \frac{\pi}{2} (\tau_{\text{rise}} + \tau_{\text{decay}}), \end{aligned} \quad (7)$$

Lastly, the asymptotic root-mean-square (RMS) amplitude of a DHO process (σ_{DHO}), which is jointly determined by the parameters in the LHS and RHS of Equation 1, can be computed using (Brockwell 2001),

$$\sigma_{\text{DHO}} = \sqrt{\frac{\beta_1^2 \alpha_2 + \beta_0^2}{2\alpha_1 \alpha_2}} = \sigma_\epsilon \sqrt{\frac{\omega_0^2 \tau_{\text{perturb}}^2 + 1}{2\xi \omega_0^3}}. \quad (8)$$

3.2. DHOs as GPs

For a given time series (light curve), CARMA (DHO in this work) parameters are commonly extracted by

⁹

We note that the driving component PSD presented here is not necessarily representative of that for the true underlying physical process, rather the features embedded (e.g., τ_{perturb}) in this PSD will inform us about important characteristics of the true physical model. We refer interested readers to Jones & Ackerson (1990), Brockwell (2001), and Kasliwal et al. (2017) for further details on the analytic form of DHO's PSD.

maximum likelihood, where the likelihood function can be calculated through Kalman recursion in the “state-space” of CARMA (Jones & Ackerson 1990; Brockwell 2001; Kelly et al. 2014; Kasliwal et al. 2017). Recently, Foreman-Mackey et al. (2017) introduced a new algorithm for performing fast Gaussian process (GP) modeling and suggested that the likelihood function of CARMA processes can be computed in $\mathcal{O}(NJ^2)$ based on this new algorithm (N is the number of data points in a time series and J is the autoregressive order (p) of a CARMA model); this new algorithm is also up to 10 times faster than the Kalman recursion method. In this work, we adopt the algorithm introduced by Foreman-Mackey et al. (2017) and express DHO processes as a special class of GPs.

Although rarely recognized, a CARMA process driven by Gaussian noise (i.e., $\epsilon(t)$ is Gaussian) is a Gaussian process, which makes it viable to calculate the likelihood function of CARMA models using GPs. The speedup demonstrated in Foreman-Mackey et al. (2017) originates from the fact that the CARMA auto-covariance function can be formulated as a sum of complex exponentials allowing the covariance matrix to be semi-separable, thus enabling faster computation of the likelihood function (Ambikasaran 2015; Foreman-Mackey et al. 2017). Below we demonstrate how to represent a DHO's auto-covariance function (or entries in the auto-covariance matrix for discretely sampled data) in terms of `celerite` kernels—the actual implementation of the algorithm presented in Foreman-Mackey et al. (2017). The full derivation for CARMA processes of all orders is beyond the scope of this work and can be found in (Yu et al. 2022, in preparation).

From Equation 4 in Kelly et al. (2014), we can write out the auto-covariance function of a DHO process,

$$R(\tau) = A_1 e^{r_1 \tau} + A_2 e^{r_2 \tau}, \quad (9)$$

$$\begin{aligned} A_1 &= \frac{(\beta_0 + \beta_1 r_1)(\beta_0 - \beta_1 r_1)}{-2 \text{Re}(r_1) * (r_2 - r_1)(r_2^* + r_1)}, \\ A_2 &= \frac{(\beta_0 + \beta_1 r_2)(\beta_0 - \beta_1 r_2)}{-2 \text{Re}(r_2) * (r_1 - r_2)(r_1^* + r_2)}, \end{aligned} \quad (10)$$

where r_1, r_2 are the two roots of the characteristic polynomial associated with the LHS of Equation 1 and τ is the positive time lag between any two timestamps. Note that Kelly et al. (2014) factored out β_0 and called it σ —equivalent to σ_ϵ defined in the previous section.

When r_1, r_2 are real (overdamped DHOs: $\xi > 1$), A_1, A_2 are also real, and Equation 9 becomes a sum of two real exponential GP kernels (`celerite` real term). In the `celerite` framework, Equation 9 for overdamped

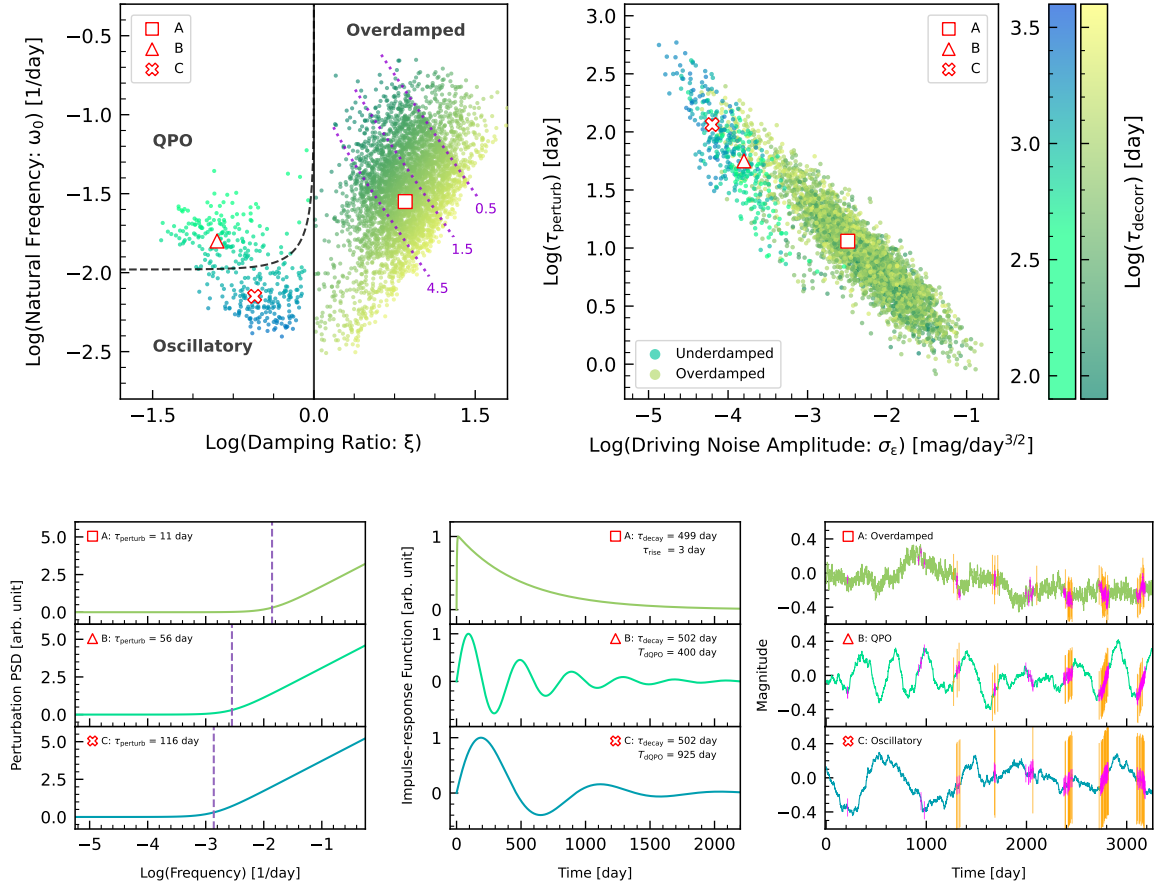


Figure 3. *Top left:* DHO fits of S82 quasars in the ξ , ω_0 space (LHS of Equation 3). Underdamped DHOs are located to the left of the solid vertical line ($\xi = 1$) and overdamped DHOs are located to the right of this same line. The dash-dotted line further (empirically) separates underdamped DHOs into QPOs and oscillatory DHOs. Both underdamped and overdamped DHOs are colored by their decorrelation timescales (τ_{decorr}) but using two different color maps. The purple dotted lines on the underdamped population show the evolution of τ_{rise} across the parameter space, where the numbers give the τ_{rise} in the unit of days. *Top right:* DHO fits of S82 quasars in the σ_ϵ , τ_{perturb} space (RHS of Equation 3). Same as in the top left panel, color shows the corresponding τ_{decorr} for each object and different color maps are used for the underdamped and overdamped populations. *Bottom left:* The driving process (RHS of Equation 3) PSDs of the three selected points **A**, **B** and **C** shown in the top two panels⁹. *Bottom center:* The response functions (LHS of Equation 3) due to a delta function impulse of the dynamical systems described by the same selected points **A**, **B** and **C**. *Bottom right:* DHO light curves simulated using **A**, **B** and **C** as the input model parameters. Superimposed are the versions downsampled using the best (magenta) and the worst (orange) cadences of our SDSS light curves (in terms of the number of observations, baseline duration, and photometric accuracy) for each classification. Median photometric uncertainties are used for error bars.

DHOs can be written as:

$$k(\tau_{nm}) = \sigma_n^2 \delta_{nm} + a_1 e^{-c_1 \tau_{nm}} + a_2 e^{-c_2 \tau_{nm}} \quad (11)$$

where τ_{nm} is the positive time lag between the n^{th} and m^{th} data point in a time series, σ_n is the measurement uncertainty on the n^{th} data point; $a_1 = A_1$, $a_2 = A_2$, $c_1 = -r_1$, and $c_2 = -r_2$. Note that for a discretely sampled DHO process, $k(\tau_{nm})$ gives the entries in the corresponding auto-covariance matrix.

In the case of underdamped DHOs ($\xi < 1$), r_1, r_2 are complex conjugates, so are A_1, A_2 . Equation 9 becomes

a single complex exponential kernel:

$$k(\tau_{nm}) = \sigma_n^2 \delta_{nm} + \frac{1}{2} (a + ib) e^{-(c+id)\tau_{nm}} + \frac{1}{2} (a - ib) e^{-(c-id)\tau_{nm}} \quad (12)$$

where $a = 2 * \text{Re}(A_1)$, $b = 2 * \text{Im}(A_1)$, $c = -\text{Re}(r_1)$, and $d = -\text{Im}(r_1)$. Given this mapping from a DHO's auto-covariance function to `celerite`'s GP kernels, we can take advantage `celerite` to fit DHO to our light curves.

3.3. Fitting DHO to Quasar Light Curves

In the previous section, we demonstrated that the `celerite` framework can be utilized to compute the likelihood function of CARMA (used DHO as an example), however, the native `celerite` software does not come with the functionality (the actual code) to fit an arbitrary CARMA model that is more complex than the DRW to light curves. To facilitate general-purpose CARMA modeling taking advantage of `celerite`, we implemented the appropriate mapping from the CARMA parameterization to the `celerite` parameterization in a new Python package—`EzTao`, which was used to fit DHO to our quasar light curves.

The likelihood landscape of a complex GP kernel (such as that of a DHO) is usually non-convex (e.g., having multiple local optima). Thus, during the fitting process we randomly initialized 100 optimizers across the DHO parameter space that can be probed by the temporal sampling of the input light curves and selected the maximum *a posteriori* (MAP) estimation as the best-fit solution, where very broad flat priors were used to prevent the potential numerical overflow/underflow caused by catastrophic runaways of the optimizers¹⁰. We performed the fitting process 5 times for each light curve to make sure that a robust fit was obtained. Our experience showed that neither increasing the number of optimizers nor repetitions will change the final distribution of the best-fit DHO parameters for our quasar sample.

After we obtained the best fit for each object, we used `emcee` (Foreman-Mackey et al. 2013), a python implementation of Goodman & Weare’s Affine Invariant Markov chain Monte Carlo (MCMC) Ensemble sampler (Goodman & Weare 2010), to sample the posterior distribution with the MCMC walkers initiated at the MAP position. One additional prior was used to restrict the MCMC walkers from potential catastrophic runaways: $10^{-3} \text{ days} < \log(\tau_{\text{perturb}}) < 10^5 \text{ days}$. We ran MCMC for 15,000 steps using 32 walkers and discarded the first 3,000 steps as the “burn-in”. The largest autocorrelation time for all chains is around 500 steps. The uncertainty of the best-fit DHO parameter is taken as the “1-sigma” range (one half the central 68.3% interval) of the marginalized posterior distribution.

4. BEST-FIT DHO PARAMETERS

¹⁰ The AR coefficients (α_1 and α_2 from the LHS of Equation 1) have a boundary of $[-15, 15]$ in the natural log scale, and the MA coefficients (β_0 and β_1 from the RHS of Equation 1) have a boundary of $[-23, 7]$ in the natural log scale

4.1. The Distribution of DHO Parameters and The Identification of Bad Fits

Just because a fit is robust (in that it does not change across multiple independent runs) does not mean that it is accurate and precise. We identified two main “dead zones” in the DHO parameter space that are hosts of bad DHO fits, these are MAP fits that are catastrophic failures potentially as a result of insufficient temporal sampling or large photometric uncertainty. DHO fits that end up in those regions, as listed below, were flagged as bad and removed from our sample:

1. DHO fits corresponding to timescales (see Section 3.1) that are either longer than the span of the light curve ($\text{Max } \Delta t$)¹¹ or shorter than one half the minimum separation between any two observations ($\text{Min } \Delta t$).
2. DHO fits with $\log(\xi) - \log(\omega_0) > 1$; for those objects, the daily observing cadence exhibits a stronger signal than the intrinsic timescales (see Figure 4).

The first cut above alone removed $\approx 70\%$ of the objects from our initial sample in every photometric band. Independently from the first cut, the second cut alone removed $\approx 55\%$ of all objects in *u* and *z*, and $\approx 20\%$ of all objects in *gri*. After these two cuts, we were left with 2997, 4570, 3530, 2999, 1180 DHO fits in *ugriz* bands, respectively. Next, we used an isolation forest (an outlier detection algorithm) (Liu et al. 2008) to further identify and remove bad fits. An isolation forest takes a data set and splits it randomly until no more split can be made. If anomalies/outliers are rare and different from the main population, it would take longer (more splits) to isolate a “regular” data point than an outlier. Therefore, those that are first isolated are identified as outliers by an isolation forest. Running an isolation forest on the current sample of DHO fits in each band separately removed an additional 5% of objects, our final sample contains 2847, 4341, 3353, 2849, 1121 good DHO fits in *u, g, r, i, z* bands, respectively.

The distribution of good DHO fits (using *g*-band as an example) is shown in the top two panels of Figure 3: the top left panel shows the distribution in the ξ, ω_0 space (the response component, LHS of Equation 3) and the top right panel shows that in the $\sigma_\epsilon, \tau_{\text{perturb}}$ space (the

¹¹ This cut will bias the distribution of τ_{decorr} , which has a median of 1000 days in the observed-frame—comparable to the baseline of our light curves. However, we stress that such a cut is needed since an intrinsic decorrelation timescale longer than the light curve span can not be constrained. See Kozłowski (2017, 2021) for close examinations of this effect on the DRW model.

driving perturbation component, RHS of Equation 3). In the top left panel of Figure 3 we can identify two main clusters, one for underdamped DHOs ($\log(\xi) < 0$) and one for overdamped DHOs ($\log(\xi) > 0$), separated by the vertical solid line at $\log(\xi) = 0$. The clustering of underdamped/overdamped populations is not a characteristic of the DHO model rather that of the quasar light curves, that is, any point in the DHO parameter space constitutes a valid model. We can further classify underdamped DHOs into quasi-periodic (QPO) and oscillatory DHOs with a (empirically chosen) dividing T_{dQPO} of 600 days (dashed line). Despite both being underdamped, QPOs generally have larger natural oscillation frequencies (ω_0) and smaller damping ratios than oscillatory DHOs. Both underdamped and overdamped DHOs are colored by their τ_{decorr} but using different color maps. The dotted purple lines on top of the overdamped population demonstrate the evolution of τ_{rise} across the response parameter space, where the numbers give the τ_{rise} in the unit of days. In the top right panel (the perturbation parameter space), objects are also colored by τ_{decorr} . Since we do not see an obvious color gradient as τ_{perturb} increases (or decreases) in the overdamped cluster, we argue that τ_{decorr} and τ_{perturb} are largely uncorrelated for overdamped DHOs, which suggests that the perturbation component (RHS of Equation 3) and the response component (LHS of Equation 3) of the modeled quasars might be decoupled. Such decoupling is expected if the perturbation process is external to instead of originating in the accretion disk of AGN (see Section 6 for further discussion).

Three representative points are chosen from the distribution of good DHO fits, one for each identified class: overdamped DHO, QPO, and oscillatory DHO, to investigate/visualize the intrinsic variability signatures embedded in the DHO parameters; they are labeled using a square (overdamped DHO), triangle (QPO), and a cross (oscillatory DHO). The bottom three panels of Figure 3, from left to right, show the perturbation spectrum—the driving process PSD (RHS of Equation 3), the impulse-response function (LHS of Equation 3), and the final (simulated) DHO light curves, of the dynamical systems described by the corresponding DHO parameters at the selected points.

It can be clearly seen from these three example DHOs that different regions of the parameter space correspond to different unique characteristics. The underdamped population— $\log(\xi) < 0$ in the top left panel of Figure 3 and the top-left corner in the top right panel of Figure 3—has large τ_{perturb} and the light curve is smooth at short timescales but bumpy at long timescales; comparatively, the QPO subclass shows a much stronger peri-

odicity than the oscillatory subclass. On the other hand, the overdamped population— $\log(\xi) > 0$ in the top left panel of Figure 3 and the bottom-right portion in the top right panel of Figure 3—has smaller τ_{perturb} and the light curve is bumpy at short timescales but smooth over large timescales.

Next, to confirm that our bad-fit identification procedure works as expected, we simulated $\sim 12,000$ DHO light curves sampled at the exact temporal cadence and photometric accuracy of the quasars in our **main sample**, and then fitted them with DHO. The input model parameters for the simulated light curves were drawn from the distribution of g -band good fits (see top two panels Figure 3). Figure 4 shows the distribution of the MAP best fits obtained on these simulated data in the ξ , ω_0 parameter space. Based on the quality cuts described at the beginning of this section, DHO fits that passed the cuts are color-coded by the difference in $\log(\omega_0)$ between the MAP value and the input; the simulated overdamped DHOs that failed to pass the cuts are shown using gray dots whereas the failed underdamped DHOs are shown using magenta crosses. We can see that the distribution of the identified good fits largely overlaps that of their input outlined by the red contour. We can also see that the bad fits that were simulated as overdamped DHOs spread over the whole ξ , ω_0 parameter space and the bad fits that were simulated as underdamped DHOs are more concentrated around the distribution of their input. The orange dashed line at the top left corner corresponds to a T_{QPO} of one day suggesting that best fits accumulated in this region might be fitting the daily observing cadence rather than the intrinsic timescales in the quasar light curves. A cut of $\log(\xi) - \log(\omega_0) > 1$ (the cyan dash-dotted line in Figure 4) effectively removes those suspicious fits. Given the resulting distribution of good/bad fits obtained on simulated light curves, we can confirm that the good fits identified through the criteria established at the start of this section are effective. However, we do find two flavors of overestimation/underestimation from the distribution of good fits: a systematic offset (between the colored distribution and the red contour) and a parameter-dependent trend (the color gradient within the colored distribution); we will discuss both scenarios with more detail in the next section.

4.2. The Effects of Time Sampling and Photometric Accuracy on Best-fit Parameters and Possible Corrections

It has been previously reported that the accuracy/precision of the maximum likelihood estimate of DRW parameters is sensitive to the “quality” of the

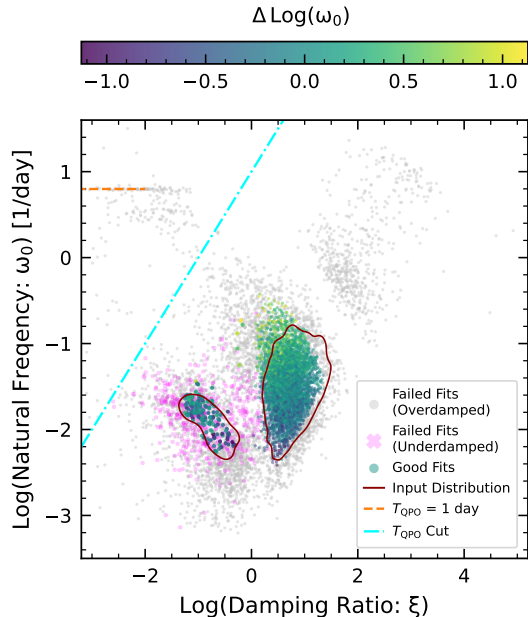


Figure 4. DHO fits for realistically simulated SDSS S82 light curves, the input model parameters are drawn from the distribution shown in the top two panels of Figure 3. The DHO fits that are identified as good using the algorithm described at the beginning of Section 4.1 are color-coded by the difference between their best-fit $\log(\omega_0)$ and the input. Identified bad fits that were simulated as overdamped DHOs are shown using gray dots and those simulated as underdamped DHOs are shown using magenta crosses. The orange dashed line marks a $T_{\text{QPO}} = 1$ day. The cyan dash-dotted line shows the cut used to remove the bad fits associated the daily observing cadence (surrounding the orange dashed line). The red contour outlines the distribution of the input DHO parameters.

light curves, more specifically, the ratio between the DRW decorrelation timescale (τ_{DRW}) and the light curve length ($\text{Max } \Delta t$) (Kozłowski 2017, 2021). DHO and DRW are the same class of stochastic diffusion processes—CARMA, thus we expect similar trends to appear for best-fit DHO parameters determined by maximum likelihood (or maximum *a posteriori* with wide flat priors).

The light curve “quality” measurements used in (Kozłowski 2017) depend on both the true parameters of the underlying process (e.g., τ_{DRW}) and some basic properties of the light curve data (e.g., $\text{Max } \Delta t$), where the former are hardly known but the latter are easily measurable. Thus, rather than trying to fully characterize the accuracy/precision of our best-fit DHO parameters with respect to those “quality” metrics, we attempted to calibrate the best-fit DHO parameters using simulated data. The same simulation process as de-

scribed at the end of Section 4.1 was carried out for all five bands, and the best-fit parameters from different bands were joint together to determine the correction. We first modeled the offset of the best-fit DHO parameters on simulated light curves relative to the input parameters ($\log(X_{\text{Output}}) - \log(X_{\text{Input}})$) as a multivariate linear function of three basic properties of the light curves: the total length of the light curve ($\text{Max } \Delta t$), the minimum separation between any two observations ($\text{Min } \Delta t$), and the median photometric uncertainty. The coefficients of the best-fit linear regression suggest that the offset is most correlated with the median photometric uncertainty and $\text{Max } \Delta t$ —consistent with the results from previous work for DRW (Kozłowski 2017).

By applying a correction derived from the best-fit multivariate regression, we were able to remove the systematic offset between the input and the output distribution of DHO parameters. The top six panels of Figure 5 show the comparison between the input parameters and the output (MAP best-fit) parameters before (orange) and after (blue) the applied correction; the middle six panels show the distributions of the offsets ($\log(X_{\text{Output}}) - \log(X_{\text{Input}})$). The corrected fits have better correspondence with the input parameters than the original ones (i.e., the blue histograms in the second row are more centered at zero than the orange ones). The panels on the third row of Figure 5 show the offsets of the corrected best fits as a function of the input parameters; any parameter-dependent trends as shown were not accounted for in our correction and are left for future investigations. From simulations, we can see that given the light-curve cadence and photometric accuracy of S82 quasars, σ_{DHO} , τ_{perturb} , and σ_{ϵ} are best constrained among all other DHO features—in terms of the size of the dispersion and the level of the parameter-dependent trend (modulo the extremes) of the offsets.

In addition to the overestimation/underestimation of DHO parameters, it would be interesting to investigate how reliable is the DHO subclass classification (underdamped DHO vs. overdamped DHO) given the light-curve cadence and photometric accuracy of S82 quasars. Using the simulated data introduced above, we computed the classification precision (and recall) for both populations. Given a clean sample, for a particular classification, the precision is defined by the percentage of best-fit DHOs that are also simulated with the same classification (e.g., a best-fit overdamped DHO is also simulated as an overdamped DHO) and the recall is defined by the percentage of simulated DHOs that are correctly classified. The final result is shown in Table 1. Since the classification of underdamped DHOs into QPOs and oscillatory DHOs is based on an empir-

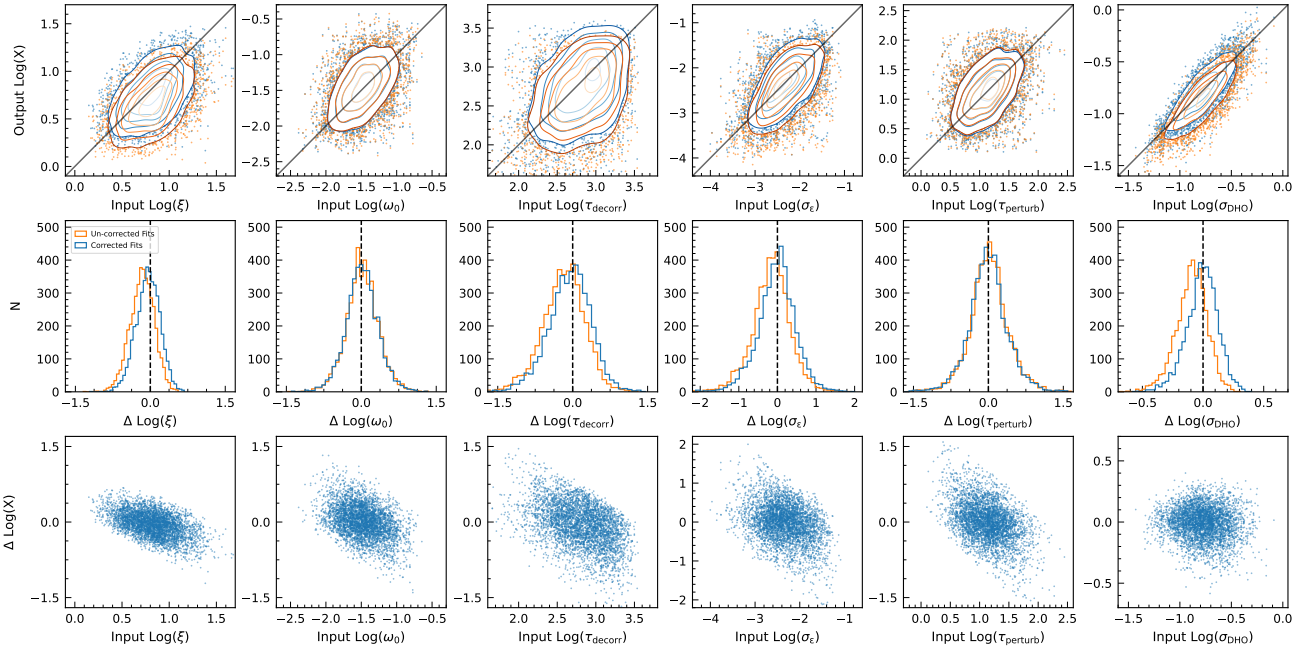


Figure 5. A comparison between the output DHO parameters obtained on simulated light curves and the true input; only simulations of overdamped DHOs are shown. Two versions of the output parameters are shown: the first one (orange) is the original MAP best fit and the second (blue) has the linear correction applied. The correction is determined from modeling the difference between the output and the input parameters in the form of $\Delta \log(X) = \log(X_{\text{Output}}) - \log(X_{\text{Input}})$, as a function of the temporal sampling and photometric accuracy of the light curves. *Row One:* Scatter plots comparing the output DHO parameters (y-axis) with the input parameters (x-axis). Solid diagonal lines show a one-to-one correspondence. *Row Two:* Histograms showing the difference between the output DHO parameters and the input. The vertical dashed lines mark an offset of zero meaning the output is in perfect agreement with the input. *Row Three:* The difference between the (corrected) output parameters and the input parameters as a function of the input parameters.

ically chosen diving T_{dQPO} , it is not as informative to show the statistics for those two classes.

Table 1. DHO Classification Precision (Recall)

band	Underdamped DHO	Overdamped DHO
u	14.29 (100.00)	100.00 (90.65)
g	29.80 (100.00)	100.00 (97.56)
r	29.46 (92.68)	99.93 (97.90)
i	24.16 (100.00)	100.00 (96.58)
z	9.18 (100.00)	100.00 (87.85)

In summary, given the temporal sampling and photometric accuracy of SDSS Stripe 82 quasar light curves, more than 99.9% of the overdamped DHOs have the correct classification across all five SDSS bands. Among those classified as underdamped DHOs, the precision is between $\approx 9\%$ and $\approx 29\%$ with the highest in the g and r bands and the lowest in the z band. The recall for the overdamped population is between $\approx 88\%$ and $\approx 98\%$ with the highest in the g and r bands and the lowest in the z band, and for the underdamped population all bands have a recall of 100% except for the r band (92.68%). Since failed overdamped DHO fits can end up

in the region of the underdamped population and failed underdamped DHO fits tend to stay close to their input (see grey dots and magenta crosses in Figure 4), we suspect that the low classification precision of the underdamped population is partially caused by the overabundance of the overdamped population. That said, given that our input parameters were drawn from the distribution of MAP best fits obtained on real SDSS Stripe 82 quasar light curves, the true relative abundance and classification precision of underdamped DHOs should be smaller than what we are showing in Figure 3 and Table 1.

5. CORRELATIONS OF DHO PARAMETERS WITH WAVELENGTH AND PHYSICAL PROPERTIES OF AGN

We investigated the correlations between the best-fit DHO parameters (corrected using the linear coefficients determined in Section 4.2) and the estimated physical properties of the quasars in our sample (Shen et al. 2011; Rankine et al. 2020). Our investigation was focused on the overdamped population provided that the classification for underdamped DHOs is highly unreli-

able (see Table 1). We also limited our analysis to three DHO features: σ_{DHO} , σ_{ϵ} and τ_{perturb} , because they are best constrained given the light-curve cadence and photometric accuracy of SDSS Stripe 82 quasars (see Figure 5) and that they are least affected by our initial timescale-based cut for removing bad DHO fits (the first criterion listed at the start of Section 4.1). More specifically, the distribution of τ_{perturb} lies between $\text{Min } \Delta t$ and $\text{Max } \Delta t$, thus, is not affected by the cuts associated with those two timescales. On the other hand, τ_{rise} is on the scale of $\text{Min } \Delta t$ (≈ 1 day) and τ_{decay} is on the scale of $\frac{1}{2} \text{Max } \Delta t$ (≈ 1000 days), therefore the distribution of τ_{rise} and τ_{decay} are subject to selection bias, and similarly for $\tau_{\text{decorr}} \approx \frac{\pi}{2}(\tau_{\text{rise}} + \tau_{\text{decay}})$. Lastly, through examining the MCMC samples of our good DHO fits we found that some of them have bi/multi-modal and/or very broad posterior distributions (see Appendix A for examples). We suspect this to be caused by the irregular/sparse sampling of S82 light curves that leaves certain timescales less well probed and/or the (lack of) variability of strong emission line(s) in the particular photometric bands. Further investigations are needed to verify the origin(s) of those bi/multi-modal posterior distributions. Nevertheless, we removed those objects from the following analysis using a well-defined metric (see Appendix A).

5.1. Wavelength Dependence of DHO Parameters

Given the large redshift range that our quasar sample spans and the five different photometric bands that we are utilizing in this investigation, best-fit DHO parameters should first be evaluated against and corrected for any wavelength dependence before being used to correlate with the physical properties of quasars. We explored the wavelength dependence of σ_{DHO} , τ_{perturb} , and σ_{ϵ} by first correcting them for redshift dependence and then plotting them as a function of the effective wavelength of their photometric bands in rest frame (Schneider et al. 1983). σ_{DHO} , τ_{perturb} , and σ_{ϵ} scale with redshift as $(1+z)^0$, $(1+z)^{-1}$, and $(1+z)^{3/2}$, respectively; the derivation for the redshift dependence of σ_{ϵ} can be found in Appendix B. The effective wavelength, computed based on a power-law continuum with a spectral index α_v of -0.5 , of the SDSS *ugriz* bands in the observer’s frame are 3541, 4653, 6147, 7461, and 8904 angstroms, respectively (Fukugita et al. 1996; Richards et al. 2001; Kaczmarczik et al. 2009).

Figure 6 shows σ_{DHO} , τ_{perturb} , and σ_{ϵ} as a function of the effective wavelength of their photometric bands in rest frame (λ_{RF}), the color indicates the specific pass-band from which the best-fit parameters are obtained. λ_{RF} for a given band is computed as: $\lambda_{\text{RF}} = \lambda_{\text{eff}}/(1+z)$,

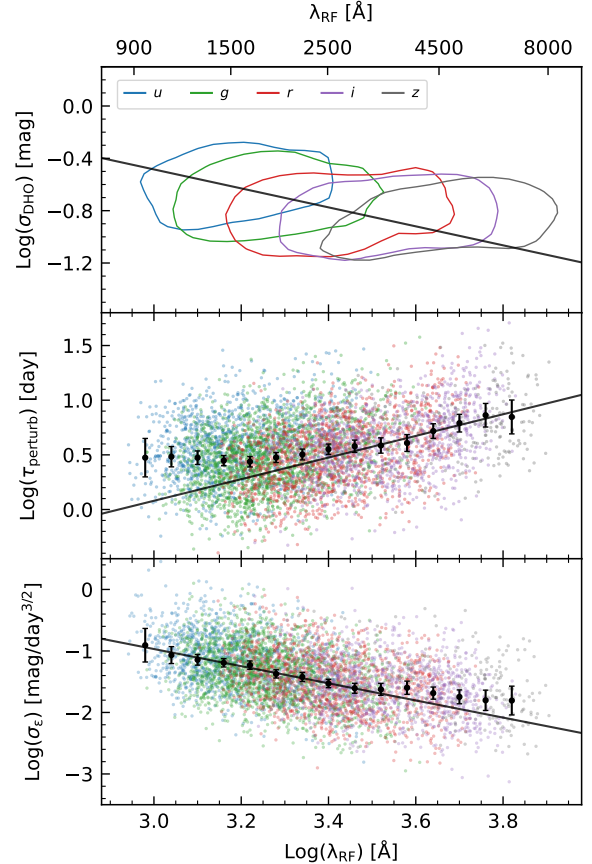


Figure 6. Distribution of σ_{DHO} , τ_{perturb} , and σ_{ϵ} as a function of rest wavelength (λ_{RF}). The color gives the photometric band from which the best-fit parameters are obtained. The black points in the middle and bottom panels mark the median values in bins centered at the corresponding λ_{RF} ; the error bars have been made twice as large for better visibility. *Top*: The contours show the 85% mass for each band. σ_{DHO} follows an overall monotonic relation with λ_{RF} ; the solid line shows the best linear fit. *Middle*: τ_{perturb} increases with λ_{RF} longward of ≈ 2500 Å; the solid line shows the best linear fit to the median values with $\lambda_{\text{RF}} > 2500$ Å. *Bottom*: σ_{ϵ} decreases with λ_{RF} shortward of ≈ 2500 Å; the solid line shows the best linear fit to the median values with $\lambda_{\text{RF}} < 2500$ Å.

where λ_{eff} is the effective wavelength in the observer’s frame and z is the redshift of an object. From the top panel we can see that σ_{DHO} follows an overall monotonically decreasing trend with λ_{RF} —in agreement with previous findings (e.g., Vanden Berk et al. 2004; MacLeod et al. 2010). We performed a bisector linear regression to derive the best-fit relation between σ_{DHO} and λ_{RF} ,

$$\log(\sigma_{\text{DHO}}) = (-0.73 \pm 0.070) \log(\lambda_{\text{RF}}) + 1.69 \pm 0.003. \quad (13)$$

Note that σ_{DHO} follows an increasing rather than a decreasing trend with λ_{RF} within each individual band.

We suspect this “misleading” increasing trend to be caused by the anti-correlation of σ_{DHO} with L_{bol} (see Section 5.2) and the selection bias intrinsic to flux-limited samples (i.e., selected objects from higher redshift are systematically more luminous than those from lower redshift).

The middle panel of Figure 6 shows that τ_{perturb} (the characteristic timescale of the perturbation component) increases with rest wavelength at $\lambda_{\text{RF}} > 2500 \text{ \AA}$ with a best-fit relation of $\log(\tau_{\text{perturb}}) = 0.99 \cdot \log(\lambda_{\text{RF}}) - 2.89$, but is nearly independent of wavelength at $\lambda_{\text{RF}} < 2500 \text{ \AA}$.

In the bottom panel of Figure 6, we see that σ_{ϵ} (the amplitude of the driving white noise) decreases with an increasing λ_{RF} until $\approx 2500 \text{ \AA}$ and then becomes nearly independent (or only weakly dependent) of wavelength. At λ_{RF} shorter than 2500 \AA , the best-fit relation between σ_{ϵ} and λ_{RF} is $\log(\sigma_{\epsilon}) = -1.39 \cdot \log(\lambda_{\text{RF}}) + 3.21$.

We note that the trends of σ_{DHO} , τ_{perturb} , and σ_{ϵ} with λ_{RF} shown in Figure 6 persist when we replace the corrected DHO parameters with their un-corrected version, however, the v-shaped correlation shown in the bottom panel for σ_{ϵ} will appear less obvious.

Both τ_{perturb} and σ_{ϵ} exhibit clearly different dependencies with wavelength on either side of 2500 \AA while σ_{DHO} only shows a largely monotonic dependency. We will further evaluate this interesting feature in Section 6.3 and discuss what could be implied regarding accretion disk models.

5.2. DHO Amplitude

The variability amplitude has been studied most extensively among all other variability metrics in terms of searching for correlations with the fundamental properties of AGN (e.g., luminosity) (Vanden Berk et al. 2004; Wilhite et al. 2007; MacLeod et al. 2010; Zuo et al. 2012). It is worthwhile to check if σ_{DHO} exhibits similar correlations with those fundamental properties of the quasars in our sample. In this part of our analysis, σ_{DHO} is corrected to a rest-frame wavelength of 2500 \AA using Equation 13, and for each quasar only the DHO fit from the photometric band with the smallest uncertainty in σ_{DHO} (determined from MCMC) is used. We also limit our quasars to $0.7 < z < 1.9$ for the sake of enforcing a consistent determination of L_{bol} , M_{BH} , and L/L_{edd} (i.e., L_{3000} was used to estimate L_{bol} and the Mg II emission line was used to estimate M_{BH} ; Shen et al. 2011). Indeed, we confirm that σ_{DHO} is anti-correlated with the recorded values of L/L_{edd} and M_{BH} for our quasars. Figure 7 demonstrates said anti-

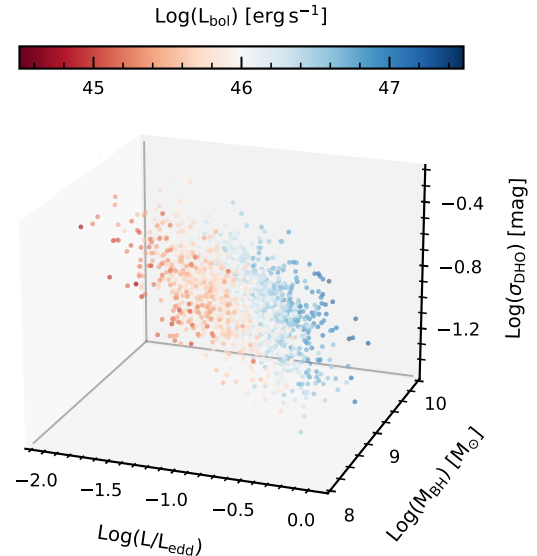


Figure 7. A 3D plot demonstrating the anti-correlations of σ_{DHO} with L/L_{edd} and M_{BH} . The x-axis is L/L_{edd} , the y-axis is M_{BH} , and the z-axis is σ_{DHO} . The color indicates L_{bol} for each object. An interactive version of this figure is available online.

correlations by displaying the distribution of our quasars in the space of σ_{DHO} , L/L_{edd} and M_{BH} . We fitted a multivariate bisector regression to σ_{DHO} , L/L_{edd} , and M_{BH} with the best-fit relation shown by Equation 14.

$$\begin{aligned} \log(\sigma_{\text{DHO}}) = & (-0.41 \pm 0.012) \log(L/L_{\text{Edd}}) \\ & + (-0.30 \pm 0.011) \log(M_{\text{BH}}) \\ & + (+1.48 \pm 0.092) \end{aligned} \quad (14)$$

Note this trend can also be expressed equivalently as an anti-correlation with L_{bol} in addition to a relatively weaker positive correlation with M_{BH} (Wilhite et al. 2007; MacLeod et al. 2010; Zuo et al. 2012).

We further explored the correlations between DHO amplitude and emission line properties, more specifically with the “Eigenvector 1” (EV1; Boroson 2002) sequence and CIV equivalent width (EQW) and blueshift. EV1 refers to a dominant trend observed among mainly low redshift AGN: the stronger the broad Fe II emission, the weaker the narrow [O III] emission. Following the convention established in Shen & Ho (2014), we define the strength of the broad Fe II ($4434\text{-}4684 \text{ \AA}$) emission as the ratio between the broad Fe II EQW and H β EQW, $R_{\text{Fe II}} = \text{EQW}_{\text{Fe II}}/\text{EQW}_{\text{H}\beta}$; the [O III] strength is characterized by its equivalent width. The left panel of Figure 8 shows the distribution of our quasars in the EV1 parameter space; we binned our sample onto a uniform grid with the color indicating the average DHO ampli-

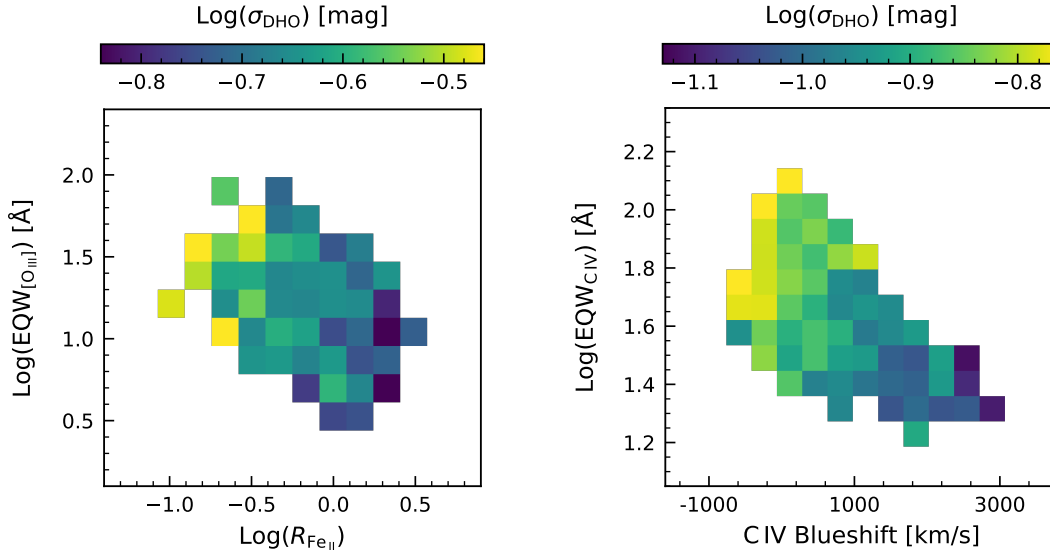


Figure 8. DHO amplitude (σ_{DHO}) and emission line properties. *Left:* Distribution of quasars in the EV1 parameter space with the color showing the mean σ_{DHO} of objects in the corresponding bins; a trend of increasing σ_{DHO} towards the top left corner is clearly shown. *Right:* Distribution of quasars in the CIV parameter space with the color showing the mean σ_{DHO} of objects in the corresponding bins; a trend of increasing σ_{DHO} with decreasing CIV blueshift and increasing CIV EQW is shown.

tude. In addition to the expected anti-correlation between $\text{EQW}_{[\text{O III}]}$ and $R_{\text{Fe II}}$, we see a trend of increasing σ_{DHO} toward the top left corner of this plot—consistent with the result from an earlier investigation conducted using a smaller sample (Ai et al. 2010). The EV1 sequence has long been argued to be driven by the diversity in L/L_{edd} (Boroson 2002; Shen & Ho 2014), that is, data points at the top left corner should have smaller L/L_{edd} than those at the bottom right corner. Indeed, this argument is consistent with that implied by the anti-correlation between σ_{DHO} and L/L_{edd} .

At high redshift, CIV EQW and CIV blueshift alone are proposed to be indicators of L/L_{edd} (Shemmer & Lieber 2015; Rankine et al. 2020). The right panel of Figure 8 shows the distribution of our sample in the CIV parameter space; we used the same technique as utilized in the EV1 analysis to bin our data. We found that our quasars tend to have larger variability amplitude than average when CIV EQW is large and CIV blueshift is small (the top left corner); on the other hand, our quasars appear to have smaller amplitude than average when CIV EQW is small and CIV blueshift is large (the bottom right corner). This trend is consistent with the anti-correlation between σ_{DHO} and L/L_{edd} and the suggestions that CIV EQW and CIV blueshift are L/L_{edd} indicators (Shemmer & Lieber 2015; Rankine et al. 2020). A similar trend was also found by Rivera et al. (2020) using multi-epoch spectroscopy, where a hybrid metric combining CIV EQW and CIV blueshift

was defined to locate quasars along this trend. This hybrid metric was later referred to as the “CIV distance” (McCaffrey & Richards 2021) in Richards et al. (2021) and Rivera et al. (2021)—the CIV distance increases its value going from the top left corner to the bottom right corner along the distribution of quasars in the CIV parameter space. Thus, an anti-correlation between σ_{DHO} and CIV distance should be expected.

5.3. The Perturbation Parameters: τ_{perturb} and σ_{ϵ}

In the DHO framework, τ_{perturb} and σ_{ϵ} characterize the driving perturbation to the modeled dynamical system, where σ_{ϵ} gives the amplitude of the driving white noise and τ_{perturb} describes a characteristic timescale beyond which the perturbation process loses power (see the bottom left panel of Figure 3 for a reference of the perturbation PSD). In the context of AGN variability modeling, we could expect τ_{perturb} and σ_{ϵ} to capture the characteristics of the physical mechanisms that drive the observed UV/optical variability, which might correlate with the fundamental properties of AGN. To that end, we explored the evolution of L/L_{edd} , L_{bol} , and M_{BH} across the τ_{perturb} , σ_{ϵ} parameter space. Since τ_{perturb} and σ_{ϵ} do not increase/decrease monotonically with λ_{RF} , our analysis only used objects with $3.35 < \log(\lambda_{\text{RF}}) < 3.45$, where both τ_{perturb} and σ_{ϵ} show clear linear dependence on λ_{RF} so that we can calibrate them to the rest wavelength of 2500 Å. As with Section 5.2, we restrict the sample to $0.7 < z < 1.9$.

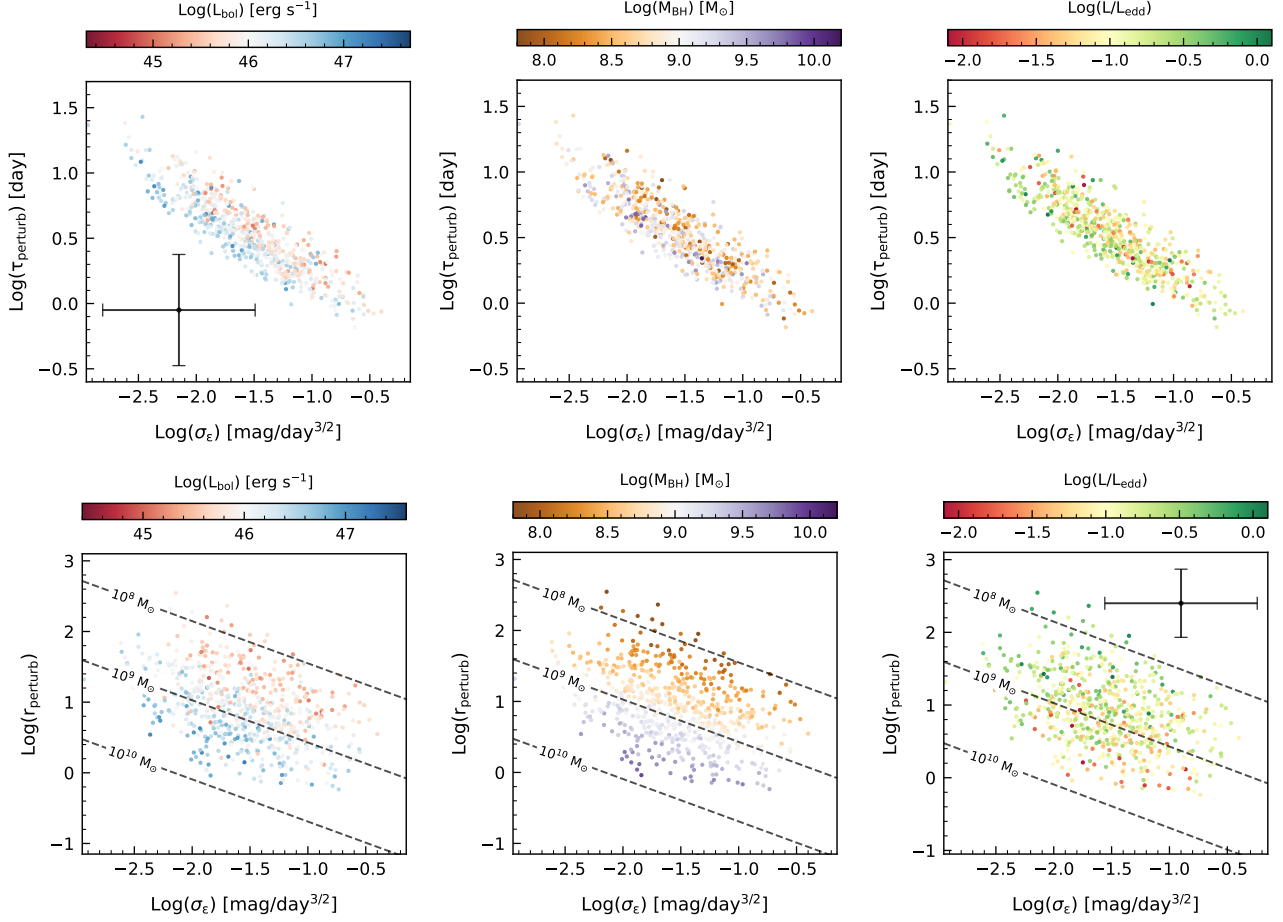


Figure 9. Distribution of quasars from $0.7 < z < 1.9$ with $3.35 < \log(\lambda_{\text{RF}}) < 3.45$ in the τ_{perturb} , σ_{ϵ} parameter space. Both τ_{perturb} , σ_{ϵ} are corrected to a rest-frame wavelength of 2500 \AA . *Top row:* From left to right, quasars are color-coded by their L_{bol} , M_{BH} , and L/L_{edd} , respectively. The median error bar is displayed at the bottom left corner of the left panel. A trend of decreasing L_{bol} with larger τ_{perturb} and σ_{ϵ} is shown in the left panel. Similar trends for M_{BH} or L/L_{edd} are not seen in the middle and right panels. *Bottom row:* Same as the top row but with the y-axis presented in the unit of gravitational radius (R_{g}) with $r_{\text{perturb}} = (\tau_{\text{perturb}} * c)/R_{\text{g}} \propto \tau_{\text{perturb}}/M_{\text{BH}}$. The median error bar is displayed at the top right corner of the right panel. The dashed lines are best-fit regression in the form of: $\log(r_{\text{perturb}}) = A * \log(\sigma_{\epsilon}) + B * \log(M_{\text{BH}}) + C$ for M_{BH} of $10^8 M_{\odot}$, $10^9 M_{\odot}$, and $10^{10} M_{\odot}$. Weighting τ_{perturb} by M_{BH} reduces the scatter seen in the top row and reveals a new trend of increasing r_{perturb} with increasing L/L_{edd} (see the bottom right panel).

The top row of Figure 9 shows the selected objects ($0.7 < z < 1.9$ and $3.35 < \log(\lambda_{\text{RF}}) < 3.45$) in the τ_{perturb} , σ_{ϵ} parameter space, and each panel, from left to right, colors objects by their L_{bol} , M_{BH} , and L/L_{edd} , respectively. In the top left panel, we can see a trend of decreasing L_{bol} toward the top right corner (large τ_{perturb} and large σ_{ϵ}); no apparent evolution of M_{BH} or L/L_{edd} across the parameter space can be found in the top middle or right panels.

Since the rest-frame τ_{perturb} is on the scale of days—comparable to the light-crossing time associated with the size of the accretion disks of our quasars—and since the characteristic radius for emission at fixed wavelengths scale linearly with M_{BH} in the log

space (Shakura & Sunyaev 1973), it is logical to convert τ_{perturb} into a distance scale (r_{perturb}) expressed in terms of gravitational radius.

$$R_{\text{perturb}} = \tau_{\text{perturb}} * c, \quad (15)$$

$$R_{\text{g}} = GM_{\text{BH}}/c^2, \quad (16)$$

$$r_{\text{perturb}} = R_{\text{perturb}}/R_{\text{g}}, \quad (17)$$

Here, c is the speed of light, G is the gravitational constant, and M_{BH} is the mass of the SMBH associated with a quasar. Thus, r_{perturb} is essentially the mass-weighted version of τ_{perturb} .

The bottom row of Figure 9 shows the distribution of the selected quasars in the r_{perturb} , σ_{ϵ} parameter space. As with the top three panels of Figure 9, from left to

right, quasars in each panel are colored by their L_{bol} , M_{BH} , and L/L_{edd} , respectively. As a guide, we plotted the best-fit regression (dashed lines) in the form of: $\log(r_{\text{perturb}}) = A*\log(\sigma_\epsilon) + B*\log(M_{\text{BH}}) + C$ for M_{BH} of $10^8 M_\odot$, $10^9 M_\odot$, and $10^{10} M_\odot$. Note that the scatter seen in the top middle panel is caused by objects with different M_{BH} having the same τ_{perturb} , weighting τ_{perturb} by M_{BH} (bottom middle panel) enables us to better see the anti-correlation of τ_{perturb} with σ_ϵ and facilitate the comparison of different objects on the same physical scale. A new trend of increasing r_{perturb} with increasing L/L_{edd} is also revealed in the bottom right panel of Figure 9. This new correlation has a non-parametric Spearman rank-order correlation coefficient of 0.35 with a two-tailed p -value of 10^{-20} .

To further elucidate the contributions of L_{bol} , M_{BH} , and L/L_{edd} to the diversity of perturbation parameters shown in Figure 9, we selected a subsample of quasars with $-1.1 < \log(L/L_{\text{edd}}) < -0.9$ and plotted their distribution in Figure 10 and colored them by their L_{bol} . From Figure 10 we can see that this subsample spans almost the full range of the distribution shown in the bottom three panels of Figure 9 and exhibits a much clearer anti-correlation (smoother color gradient) between the perturbation parameters and L_{bol} (compared to the bottom left panel in Figure 9). The large span of this subsample in the perturbation parameter space and the cleaner/smooth color gradient of L_{bol} suggest that most of the diversity in r_{perturb} (and τ_{perturb}) is driven by L_{bol} (or M_{BH}) and that L/L_{edd} works independently of L_{bol} (or M_{BH}) in terms of determining the observed distribution and plays only a minor role.

6. DISCUSSION

6.1. Underdamped DHOs: QPOs and Oscillatory DHOs

In Section 5, we omitted QPOs and oscillatory DHOs from comparing DHO features with the derived physical properties of our quasars because of their low classification precision (see Table 1). However, both subclasses exhibit interesting signatures that can be expected from real physical systems.

As the name suggests, QPOs vary quasi-periodically (see the simulated light curves in Figure 3). Such signals in quasars might be expected from super-massive black hole binaries orbiting each other closely and appearing as a single point source in the image (Begelman et al. 1980). SMBH binaries are expected to emit low-frequency gravitational waves when they merge. QPOs are most likely candidates for those systems and therefore will provide a large pool of potential sources for current and future low-frequency gravitational wave

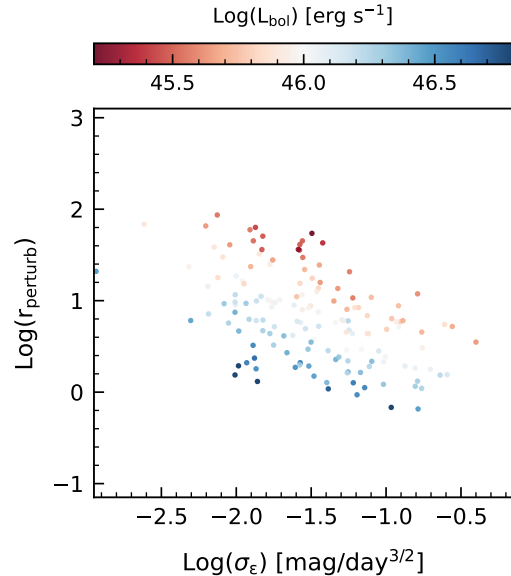


Figure 10. Quasars with $-1.1 < \log(L/L_{\text{edd}}) < -0.9$ in the r_{perturb} , σ_ϵ parameter space. A trend of decreasing L_{bol} towards the top right corner is clearly shown.

projects (Hobbs 2013; McLaughlin 2013; Amaro-Seoane et al. 2017). At the same time, persistent quasi-periodic oscillations can also be expected from single SMBHs where the inner accretion flow is geometrically thick and undergoes Lense–Thirring precession (Ingram et al. 2009; Graham et al. 2015).

Oscillatory DHOs feature larger τ_{perturb} and smaller σ_ϵ compared to overdamped DHOs (see the top right panel of Figure 3). If most of the variability in overdamped DHOs can be attributed to X-ray reprocessing (which will be discussed further in Section 6.2), then the variability revealed in oscillatory DHOs might originate in the local accretion disk. More specifically, the larger τ_{perturb} and smaller σ_ϵ could be interpreted as characteristics of a perturbation mechanism different than X-ray illumination, e.g., changes in the mass accretion rate, which might feature a longer characteristic perturbation timescale (τ_{perturb}) and a smaller short-term variability amplitude (σ_ϵ) (Pereyra et al. 2006; Li & Cao 2008; Arévalo et al. 2008). Such variability signatures can be expected from quasars with extremely high L/L_{edd} where the radiation from the X-ray corona is weak relative to the intrinsic radiation from the disk (Kubota & Done 2018) or blocked by a puffed up inner disk (see Figure 15 from Leighly (2004) or Figure 18 from Luo et al. (2015) for a reference), both would lead to little or no X-ray reprocessing.

Besides these extreme objects, we might expect to see a mixture of signatures from both an oscillatory DHO and an overdamped DHO in real light curves,

that is, assuming that intrinsic disk variability due to changing mass accretion rate and X-ray reprocessing are contributing comparably to the observed variability (Arévalo et al. 2008). Such scenarios could also lead to bi-modal distributions in the MCMC samples (see Appendix A). In those cases, we will need more advanced modeling tools to decouple the light from different processes. Nonetheless, we have removed objects with bi/multi-modal posterior distributions from our analysis and the analysis presented in Section 5 is concentrated on the overdamped population only, therefore, it is logical to suspect that the variability features revealed in this investigation are likely dominated by one single mechanism (e.g., X-ray reprocessing).

6.2. Long-term Amplitude of Overdamped DHOs: Primarily Determined by L/L_{edd} ?

We find that the long-term asymptotic variability amplitude of AGN in the overdamped subclass, as characterized by σ_{DHO} , is anti-correlated with Eddington ratio and black hole mass. This finding is consistent with that resulted from previous investigations utilizing other methods (Vanden Berk et al. 2004; Wilhite et al. 2007; MacLeod et al. 2010; Ai et al. 2010; Simm et al. 2016). The anti-correlation of σ_{DHO} with L/L_{edd} is expected in a model where the size of the hot X-ray corona relative to the accretion disk anti-correlates with L/L_{edd} and the optical variability is largely due to reprocessing of X-ray photons (e.g., Kubota & Done 2018; Giustini & Proga 2019). More specifically, a high L/L_{edd} corresponds to a small X-ray corona and a large/strong disk, therefore, less reprocessing of X-ray photons occurs in the disk—leading to a smaller long-term variability amplitude; on the other hand, a low L/L_{edd} indicates a large X-ray corona relative to the disk, thus, more reprocessing of X-ray photons occurs in the disk and a larger long-term variability amplitude can be expected. We note that the correlations discussed in this section can also be produced by changing mass accretion rate in the disk (Li & Cao 2008), moreover, recent work on intensive multi-band AGN reverberation mapping for a handful of objects have provided potential evidence for such scenario (Edelson et al. 2017; Starkey et al. 2017; Edelson et al. 2019; Cackett et al. 2020), see Cackett et al. (2021) for more discussion on this topic.

If L/L_{edd} sets the basic level of AGN variability, then the additional anti-correlation with M_{BH} can be explained by the recognition that the part of the accretion disk that emits at a fixed effective temperature changes radius with increasing/decreasing M_{BH} . The flux emitted per unit area at a radius $R \gg 6R_{\text{g}}$ on the disk is

defined as

$$F(R) = \sigma T(R)^4 \propto (\dot{m}/M_{\text{BH}})(R/R_{\text{g}})^{-3} \propto \dot{m}M_{\text{BH}}^2R^{-3}, \quad (18)$$

where T is the effective temperature at a radius R , \dot{m} is the Eddington ratio, M_{BH} is the black hole mass, and R_{g} is the gravitational radius (Novikov & Thorne 1973). According to this equation, the radius (R) on the disk that emits at a fixed temperature (a fixed wavelength), given a known Eddington ratio, moves outwards with increasing M_{BH} resulting in a larger distance to the illuminating X-ray corona. In a ‘lamppost’ geometry, the larger the distance to the X-ray corona, the smaller the intensity of the illuminating X-ray photons and the smaller the variability amplitude due to X-ray reprocessing. Therefore, we argue that the variability amplitude could be largely determined by L/L_{edd} with M_{BH} acting as a secondary parameter.

6.3. Perturbation Parameters of Overdamped DHOs: Indicating a Two-component Accretion Disk?

In Figure 6, we saw that τ_{perturb} and σ_{ϵ} do not strictly follow a power-law relation with λ_{RF} with a break point at $\approx 2500 \text{ \AA}$; the change in dependency with λ_{RF} could signify that two different physical processes are involved in shaping the observed variability. Our speculation can be explained by a physical model of the accretion flow consisting of: a hot X-ray corona extending from the innermost stable circular orbit (ISCO) to the inner edge of a truncated disk ($r_{\text{hot}} = R_{\text{hot}}/R_{\text{g}}$), a warm Comptonization region (for producing the soft X-ray excess) spanning from r_{hot} to an intermediate radius ($r_{\text{warm}} = R_{\text{warm}}/R_{\text{g}}$), and a standard cold thin disk going from r_{warm} to the outer edge of the disk (Rózańska & Czerny 2000; Czerny et al. 2003; Sobolewska et al. 2004; Done et al. 2012; Kubota & Done 2018). In this model, the warm Comptonization region features two slabs of warm electrons sandwiching the standard disk; it is also assumed that the hot X-ray corona is the main driver of the UV/optical variability. A schematic view of said geometry is shown in Figure 11, where the blue annulus represents the hot X-ray corona, the green slab represents the warm Comptonization region, and the purple slab corresponds to the outer standard disk. Note that the disk does not extend to the ISCO and truncates at r_{hot} .

More concretely, given this two-component accretion disk model (warm Comptonization region + standard thin disk region) and the fact that the effective temperature of a disk annulus scales with its radius (see Equation 18), we might suspect the observed break point (at $\approx 2500 \text{ \AA}$) in the wavelength dependence of τ_{perturb} and

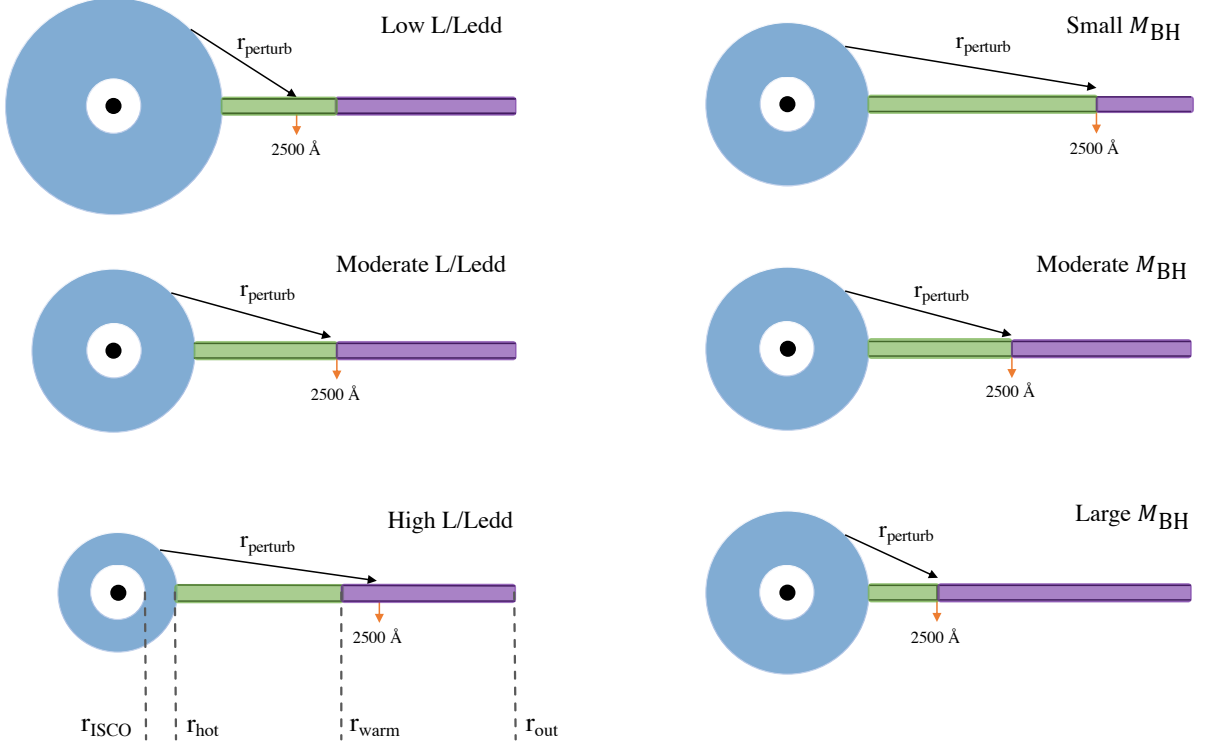


Figure 11. Diagrams providing schematic views of the accretion disk geometry proposed in Kubota & Done (2018) for a variety of L/L_{edd} and M_{BH} . Note that the diagrams are drawn in the units of gravitational radius and Equation 18 is used as a reference when discussing the changing disk geometry. The blue annulus represents the hot X-ray corona, the green slab shows the warm Comptonization region of the disk, and the purple slab corresponds to the standard disk region. The effective emitting wavelength of the disk increases going from r_{hot} to r_{out} . The r_{perturb} arrow connects the X-ray corona to the disk annulus emitting at an effective wavelength of 2500 \AA . *Left column:* M_{BH} is held fixed and L/L_{edd} increases from top to bottom. The size of the X-ray corona decreases and the 2500 \AA mark shifts outwards with increasing L/L_{edd} . The effective temperature/wavelength of the disk at the boundary between the warm Comptonization region (green slab) and the standard disk region (purple slab) also increases/decreases with L/L_{edd} . *Right column:* L/L_{edd} is held fixed and M_{BH} increases from top to bottom. When L/L_{edd} is fixed, the disk temperature (wavelength) at the boundary between the green and purple slab should stay relatively fixed, thus, increasing M_{BH} shifts both r_{warm} and the 2500 \AA disk annulus inwards.

σ_ϵ to correlate with the transition point from the warm Comptonization region to the standard disk region. At $r > r_{\text{warm}}$ (or $\lambda_{\text{RF}} > 2500 \text{ \AA}$ given our data), the hot X-ray corona directly illuminates the disk, and τ_{perturb} probes the light-crossing time between the emitting disk annulus and the corona. At $r < r_{\text{warm}}$ (or $\lambda_{\text{RF}} < 2500 \text{ \AA}$ given our data), the hot X-ray photons are scattered by the warm electrons in the upper atmosphere of the disk, therefore, the perturbation process exhibits an increased τ_{perturb} from that expected for direct illumination (see the best-fit line and the median values in the middle panel of Figure 6). At the same time, the down-scattered photons (with reduced frequencies) are better absorbed at the disk surface compared to the source X-ray photons because the absorption coefficients for both free-free and bound-free absorptions are inversely proportional to frequency (Rybicki & Lightman 1986), which

leads to an intensified perturbation amplitude (σ_ϵ). We acknowledge that the empirically identified break wavelength of 2500 \AA is an ensemble average over the true break wavelengths for our selected quasars and that the break wavelength could shift as a function of L/L_{edd} (see the left column of Figure 11), as suggested by Kubota & Done (2018). However, the size of the error bars in our inferred parameters prohibit us from revealing it. Future investigations utilizing better light curves are needed to characterize that dependency.

The trend revealed by the bottom panel of Figure 6 for σ_ϵ and the change in behaviors at $\approx 2500 \text{ \AA}$ also agrees with the result presented in Wilhite et al. (2005), which used a composite difference spectrum constructed from ≈ 300 SDSS quasars to demonstrate a similar λ_{RF} dependency of σ_ϵ . However, such a trend is not apparent in the correlation of the long-term variability amplitude

with λ_{RF} —as shown with σ_{DHO} and other metrics (e.g., σ_{DRW} ; MacLeod et al. 2010). We suspect the missing imprint of the short-term variability amplitude (σ_ϵ) on the long-term variability amplitude (σ_{DHO}) could be related to the thermalization of the illuminating photons with the disk over long timescales. It is also possible that the correlation of the long-term variability amplitude with λ_{RF} is itself a function of L/L_{edd} and/or L_{bol} and that the quasar samples used in previous work and this one for deriving such correlation span a large range of L/L_{edd} and L_{bol} . Indeed, the quasars used in this work cover a slightly larger range, as characterized by the dispersion of the distribution, of L/L_{edd} than that used in Wilhite et al. (2005). The L/L_{edd} distribution of our quasars have a median absolute deviation (MAD) and a IQR of 0.54 dex and 0.27 dex, respectively, whereas the same statistics for quasars used in Wilhite et al. (2005) have a value of 0.43 dex and 0.22 dex, respectively. Moreover, we found σ_{DHO} to follow a similar v-shaped trend with λ_{RF} as for σ_ϵ when binned with L_{bol} or L/L_{edd} . A larger sample of quasars with trusted physical properties and high-quality light curves is needed to investigate and characterize how the correlation of σ_{DHO} with λ_{RF} depends on the value of L_{bol} and L/L_{edd} .

Based on the model proposed in Kubota & Done (2018) and the fact that we can approximate the effect of the illuminating X-ray corona at $r \gg 6$ using a point source on the spin axis at a height of $H = r_{\text{hot}}$ (Gardner & Done 2017), r_{perturb} at the break wavelength is effectively $\sqrt{r_{\text{hot}}^2 + r_{\text{warm}}^2}$, assuming it probes the distance from the X-ray corona to the disk at r_{warm} . According to the best-fit parameters for Mrk 509 and PG1115+407 shown in Table 2 of Kubota & Done (2018), $\sqrt{r_{\text{hot}}^2 + r_{\text{warm}}^2}$ should exhibit a negligible correlation with L/L_{edd} given a fixed M_{BH} . Indeed, we only see a weak trend of increasing r_{perturb} with increasing L/L_{edd} from the bottom right panel of Figure 9. We also suspect that trend as a result of incorrect break wavelength being adopted for quasars having a large range of L/L_{edd} , that is, the break wavelength should decrease with increasing L/L_{edd} and calibrating all τ_{perturb} to the λ_{RF} of 2500 Å produces a false-positive trend of increasing r_{perturb} with increasing L/L_{edd} (see the diagrams in the left columns of Figure 11). Nonetheless, the distance scale reflected by τ_{perturb} (r_{perturb} : 30–150 R_{g}) is comparable to the numbers quoted in Table 2 of Kubota & Done (2018). In addition, for a given L/L_{edd} , r_{perturb} should decrease with increasing M_{BH} (and L_{bol}), because r_{warm} (if corresponding to a constant temperature) decreases when M_{BH} increases according to Equation 18 (see the right column of Figure 11) and $H = r_{\text{hot}}$ is rel-

atively fixed for a fixed spin (Kubota & Done 2018); the selected subsample of quasars with $-1.1 < \log(L/L_{\text{edd}}) < -0.9$ as shown in Figure 10 demonstrates this correlation.

We currently do not understand the origin of the anticorrelation between r_{perturb} and σ_ϵ (at a fixed M_{BH}), but it is consistent with a picture where the closer the disk is to the X-ray corona the larger the perturbation amplitude. The most straightforward explanation is that the range of spins of the central black holes has produced the diversity in $r_{\text{perturb}}/\tau_{\text{perturb}}$ given all other parameters of the SMBH held fixed; however, further investigation is required to verify this hypothesis.

Our results lead to conclusions: 1) the warm Comptonization region might be responsible for the observed break in the wavelength dependence of τ_{perturb} and σ_ϵ ; 2) τ_{perturb} at $\lambda_{\text{RF}} > 2500$ Å might be associated with the light crossing time from the X-ray corona to the accretion disk; 3) the short-term variability amplitude decreases with wavelength at $\lambda_{\text{RF}} < 2500$ Å and stays roughly constant (or drops at a much slower rate) with rest-frame wavelength—consistent with that shown in Wilhite et al. (2005).

7. SUMMARY

In this work, we have investigated the UV/optical variability of $\approx 12,000$ SDSS S82 quasars by modeling their light curves in the *ugriz* bands as DHO processes. A DHO process can be fully described by four basic parameters: a natural oscillation frequency (ω_0), a damping ratio (ξ), a characteristic perturbation timescale (τ_{perturb}), and an amplitude for the perturbing white noise (σ_ϵ). The asymptotic (long-term) variability amplitude is characterized by σ_{DHO} (a function of the above four parameters). We explored the correlations of the best-fit DHO parameters and the derived features with the physical properties of our quasars estimated by Shen et al. (2011). The main results are summarized below:

1. The distribution of the best-fit DHO parameters splits naturally into two main clusters: an overdamped DHO population and an underdamped DHO population (see Figure 3). The overdamped population exhibits similar variability signatures as those characterized by a DRW model. The underdamped population can be further classified (empirically) into the QPO subclass and the oscillatory DHO subclass. Both QPOs and oscillatory DHOs have light curves that are smoother at short timescales (smaller ξ) but bumpier at long timescales than those of overdamped DHOs. The QPO subclass features observable quasi-periodicity in its light curve.

2. σ_{DHO} , τ_{perturb} , and σ_{ϵ} of overdamped DHOs evolve with rest-frame wavelength (λ_{RF}). σ_{DHO} follows a largely monotonic trend with λ_{RF} with a power-law index of -0.73 ± 0.070 . τ_{perturb} also follows a power-law relation with λ_{RF} but only at $\lambda_{\text{RF}} > 2500 \text{ \AA}$. For σ_{ϵ} , a clear power-law relation is only observed at $\lambda_{\text{RF}} < 2500 \text{ \AA}$.
3. After correcting for the wavelength dependence, σ_{DHO} (of overdamped DHOs) exhibits anti-correlations with both L/L_{edd} and M_{BH} —in agreement with the results of previous work (e.g., Wilhite et al. 2007; MacLeod et al. 2010). However, our best-fit regression (Equation 14) suggests steeper anti-correlations of σ_{DHO} with L/L_{edd} and M_{BH} than that reported in MacLeod et al. (2010) for a DRW model.
4. We found that the short-term variability of overdamped DHOs as parameterized by τ_{perturb} and σ_{ϵ} is anti-correlated with L_{bol} .
5. We argue that the different characteristics of AGN UV/optical variability revealed by overdamped DHOs as listed above can be connected together using a physical picture: 1) L/L_{edd} determines the size (extension) of the X-ray corona relative to the truncated accretion disk; 2) the majority of the observed variability can be attributed to the reprocessing of X-ray photons by a relatively passive accretion disk; 3) from inside out, the accretion disk is divided into two regions—a warm Comptonization region and a standard thin disk region, where the warm Comptonization region is sandwiched by layers of warm electrons that produce the soft X-ray excess (Kubota & Done 2018).

Limited by the cadence and photometric accuracy of the dataset used in this work, we are only able to investigate the correlations of three features of the overdamped DHO population with the physical properties of AGN. With light curves of better temporal sampling and/or higher photometric accuracy such as those from current/future time-domain surveys (Chambers et al. 2016; Bellm et al. 2019; Ivezić et al. 2019), we can further exploit DHO modeling in AGN variability study. For example, the QPO subclass can provide a pool of SMBH binary candidates, when utilized jointly with other SMBH binary discovery methods, both the selection efficiency and completeness can be improved (Graham et al. 2015; Liu et al. 2016; Charisi et al. 2016). In addition, oscillatory DHOs are likely candidates for AGN that accrete at extremely high L/L_{edd} , where the inner disk has puffed up to prevent the X-ray

corona from directly illuminating the disk thus resulting in a smoother light curve at short timescales (Leighly 2004; Luo et al. 2015). Moreover, the discovered anti-correlation of τ_{perturb} and σ_{ϵ} with L_{bol} , together with the known anti-correlation of σ_{DHO} with L/L_{edd} and M_{BH} (or L_{bol}), can be utilized to develop new algorithms that will derive L/L_{edd} for millions of AGN using photometric data alone. Lastly, our sample of quasars span only a limited range in M_{BH} ($10^8 M_{\odot}$ to $10^{10} M_{\odot}$), applying the same analysis technique used here to AGN of much smaller M_{BH} (e.g., $10^6 M_{\odot}$) will help further elucidate the correlations between variability and fundamental properties of AGN.

Despite the better sampling and high S/N of light curves coming from current and future time-domain surveys (Bellm et al. 2019; Ivezić et al. 2019), we stress the need to develop reliable methods that can effectively merge light curves from multiple surveys for the sake of extending the baseline. Given the current likelihood-based inference technique, the long-term variability of AGN (on the scale of years) can only be best constrained when the light curves are much longer than the intrinsic timescales (Kozłowski 2017, 2021). However, the stochastic nature of AGN variability and its correlation with wavelength make merging light curves by median/mean magnitude a sub-optimal solution. In addition to constructing longer light curves, better inference algorithms that can specifically tackle the effects of sparse sampling and short baseline for light curves will be very helpful. We also emphasize that an ultimate algorithm that can efficiently fit light curves from different bands simultaneously will be essential to perform a ‘true’ CARMA modeling of AGN light curves given that the light curves from different passbands (and the information encoded therein) should be inter-correlated (see Hu & Tak (2020) for a heuristic example of such approach).

Last but not least, stochastic diffusion processes like DRW and DHO are statistical models rather than physical models. Therefore, care should be taken when interpreting the timescales extracted from stochastic modeling. One interesting discovery that we made while comparing the DRW features and the DHO features derived from the dataset used in this work is that the decorrelation/decay timescale of DRW (τ_{DRW}) is not correlated with the decorrelation/decay timescale of DHO (τ_{decorr} or τ_{decay}) as we would have expected, but instead exhibits a tight correlation with the ratio between τ_{decay} and τ_{perturb} of DHO (see Figure 14). We discuss plausible origin(s) of this “mis-match” in Appendix C.

ACKNOWLEDGMENTS

M.S.V., G.T.R., and J.M. acknowledge support from NASA grant NNX17AF18G. We thank the referee for a thorough review and the helpful comments.

Funding for the SDSS and SDSS-II has been provided by the Alfred P. Sloan Foundation, the Participating Institutions, the National Science Foundation, the U.S. Department of Energy, the National Aeronautics and Space Administration, the Japanese Monbukagakusho, the Max Planck Society, and the Higher Education Funding Council for England. The SDSS Web Site is <http://www.sdss.org/>.

The SDSS is managed by the Astrophysical Research Consortium for the Participating Institutions. The Participating Institutions are the American Museum of Natural History, Astrophysical Institute Potsdam, University of Basel, University of Cambridge, Case Western Reserve University, University of Chicago, Drexel University, Fermilab, the Institute for Advanced Study, the Japan Participation Group, Johns Hopkins University, the Joint Institute for Nuclear Astrophysics, the Kavli Institute for Particle Astrophysics and Cosmology, the Korean Scientist Group, the Chinese Academy of Sciences (LAMOST), Los Alamos National Laboratory, the Max-Planck-Institute for Astronomy (MPIA), the Max-Planck-Institute for Astrophysics (MPA), New Mexico State University, Ohio State University, University of Pittsburgh, University of Portsmouth, Princeton University, the United States Naval Observatory, and the University of Washington.

Funding for the Sloan Digital Sky Survey IV has been provided by the Alfred P. Sloan Foundation, the U.S. Department of Energy Office of Science, and the Participating Institutions. SDSS-IV acknowledges support and resources from the Center for High Performance Computing at the University of Utah. The SDSS website is www.sdss.org.

SDSS-IV is managed by the Astrophysical Research Consortium for the Participating Institutions of the SDSS Collaboration including the Brazilian Partici-

pation Group, the Carnegie Institution for Science, Carnegie Mellon University, Center for Astrophysics — Harvard & Smithsonian, the Chilean Participation Group, the French Participation Group, Instituto de Astrofísica de Canarias, The Johns Hopkins University, Kavli Institute for the Physics and Mathematics of the Universe (IPMU) / University of Tokyo, the Korean Participation Group, Lawrence Berkeley National Laboratory, Leibniz Institut für Astrophysik Potsdam (AIP), Max-Planck-Institut für Astronomie (MPIA Heidelberg), Max-Planck-Institut für Astrophysik (MPA Garching), Max-Planck-Institut für Extraterrestrische Physik (MPE), National Astronomical Observatories of China, New Mexico State University, New York University, University of Notre Dame, Observatório Nacional / MCTI, The Ohio State University, Pennsylvania State University, Shanghai Astronomical Observatory, United Kingdom Participation Group, Universidad Nacional Autónoma de México, University of Arizona, University of Colorado Boulder, University of Oxford, University of Portsmouth, University of Utah, University of Virginia, University of Washington, University of Wisconsin, Vanderbilt University, and Yale University.

This research makes use of the SciServer science platform (www.sciserver.org). SciServer is a collaborative research environment for large-scale data-driven science. It is being developed at, and administered by, the Institute for Data Intensive Engineering and Science at Johns Hopkins University. SciServer is funded by the National Science Foundation through the Data Infrastructure Building Blocks (DIBBs) program and others, as well as by the Alfred P. Sloan Foundation and the Gordon and Betty Moore Foundation.

Software: pandas (McKinney 2010), numpy (Harris et al. 2020), scipy (Virtanen et al. 2020), matplotlib (Hunter 2007), astropy (The Astropy Collaboration et al. 2013; Astropy Collaboration et al. 2018), emcee (Foreman-Mackey et al. 2013), eztao (Yu & Richards 2022)

REFERENCES

- Abazajian, K. N., Adelman-McCarthy, J. K., Agüeros, M. A., et al. 2009, *Astrophysical Journal, Supplement Series*, 182, 543, doi: [10.1088/0067-0049/182/2/543](https://doi.org/10.1088/0067-0049/182/2/543)
- Ai, Y. L., Yuan, W., Zhou, H. Y., et al. 2010, *The Astrophysical Journal*, 716, L31, doi: [10.1088/2041-8205/716/1/L31](https://doi.org/10.1088/2041-8205/716/1/L31)
- Amaro-Seoane, P., Audley, H., Babak, S., et al. 2017, arXiv:1702.00786 [astro-ph].
<https://arxiv.org/abs/1702.00786>
- Ambikasaran, S. 2015, arXiv:1409.7852 [cs, math, stat].
<https://arxiv.org/abs/1409.7852>
- Annis, J., Soares-Santos, M., Strauss, M. A., et al. 2014, *ApJ*, 794, 120, doi: [10.1088/0004-637X/794/2/120](https://doi.org/10.1088/0004-637X/794/2/120)

- Arévalo, P., Uttley, P., Kaspi, S., et al. 2008, *MNRAS*, 389, 1479, doi: [10.1111/j.1365-2966.2008.13719.x](https://doi.org/10.1111/j.1365-2966.2008.13719.x)
- Astropy Collaboration, Price-Whelan, A. M., Sipőcz, B. M., et al. 2018, *AJ*, 156, 123, doi: [10.3847/1538-3881/aabc4f](https://doi.org/10.3847/1538-3881/aabc4f)
- Bauer, A., Baltay, C., Coppi, P., et al. 2009, *ApJ*, 696, 1241, doi: [10.1088/0004-637X/696/2/1241](https://doi.org/10.1088/0004-637X/696/2/1241)
- Begelman, M. C., Blandford, R. D., & Rees, M. J. 1980, *Nature*, 287, 307, doi: [10.1038/287307a0](https://doi.org/10.1038/287307a0)
- Bellm, E. C., Kulkarni, S. R., Graham, M. J., et al. 2019, *PASP*, 131, 018002, doi: [10.1088/1538-3873/aaecbe](https://doi.org/10.1088/1538-3873/aaecbe)
- Boroson, T. A. 2002, *ApJ*, 565, 78, doi: [10.1086/324486](https://doi.org/10.1086/324486)
- Borucki, W. J., Koch, D., Basri, G., et al. 2010, *Science*, 327, 977, doi: [10.1126/science.1185402](https://doi.org/10.1126/science.1185402)
- Bramich, D. M., Vidrih, S., Wyrzykowski, L., et al. 2008, *Monthly Notices of the Royal Astronomical Society*, 386, 887, doi: [10.1111/j.1365-2966.2008.13053.x](https://doi.org/10.1111/j.1365-2966.2008.13053.x)
- Brockwell, P. J. 2001, *Handbook of Statistics*, 19, 249, doi: [10.1016/S0169-7161\(01\)19011-5](https://doi.org/10.1016/S0169-7161(01)19011-5)
- Cackett, E. M., Bentz, M. C., & Kara, E. 2021, *iScience*, 24, 102557, doi: [10.1016/j.isci.2021.102557](https://doi.org/10.1016/j.isci.2021.102557)
- Cackett, E. M., Gelbord, J., Li, Y.-R., et al. 2020, *ApJ*, 896, 1, doi: [10.3847/1538-4357/ab91b5](https://doi.org/10.3847/1538-4357/ab91b5)
- Caplar, N., Lilly, S. J., & Trakhtenbrot, B. 2017, *ApJ*, 834, 111, doi: [10.3847/1538-4357/834/2/111](https://doi.org/10.3847/1538-4357/834/2/111)
- Chambers, K. C., Magnier, E. A., Metcalfe, N., et al. 2016, *arXiv:1612.05560 [astro-ph]*, <https://arxiv.org/abs/1612.05560>
- Charisi, M., Bartos, I., Haiman, Z., et al. 2016, *Mon. Not. R. Astron. Soc.*, 463, 2145, doi: [10.1093/mnras/stw1838](https://doi.org/10.1093/mnras/stw1838)
- Chelouche, D., & Daniel, E. 2012, *ApJ*, 747, 62, doi: [10.1088/0004-637X/747/1/62](https://doi.org/10.1088/0004-637X/747/1/62)
- Chelouche, D., Shemmer, O., Cotlier, G. I., Barth, A. J., & Rafter, S. E. 2014, *ApJ*, 785, 140, doi: [10.1088/0004-637X/785/2/140](https://doi.org/10.1088/0004-637X/785/2/140)
- Czerny, B., Nikolajuk, M., Róžańska, A., et al. 2003, *A&A*, 412, 317, doi: [10.1051/0004-6361:20031441](https://doi.org/10.1051/0004-6361:20031441)
- Done, C., Davis, S. W., Jin, C., Blaes, O., & Ward, M. 2012, *Monthly Notices of the Royal Astronomical Society*, 420, 1848, doi: [10.1111/j.1365-2966.2011.19779.x](https://doi.org/10.1111/j.1365-2966.2011.19779.x)
- Edelson, R., Gelbord, J., Cackett, E., et al. 2017, *ApJ*, 840, 41, doi: [10.3847/1538-4357/aa6890](https://doi.org/10.3847/1538-4357/aa6890)
- . 2019, *ApJ*, 870, 123, doi: [10.3847/1538-4357/aaf3b4](https://doi.org/10.3847/1538-4357/aaf3b4)
- Foreman-Mackey, D., Agol, E., Ambikasaran, S., & Angus, R. 2017, *AJ*, 154, 220, doi: [10.3847/1538-3881/aa9332](https://doi.org/10.3847/1538-3881/aa9332)
- Foreman-Mackey, D., Hogg, D. W., Lang, D., & Goodman, J. 2013, *Publications of the Astronomical Society of the Pacific*, 125, 306, doi: [10.1086/670067](https://doi.org/10.1086/670067)
- Frieman, J. A., Bassett, B., Becker, A., et al. 2008, *The Astronomical Journal*, 135, 338, doi: [10.1088/0004-6256/135/1/338](https://doi.org/10.1088/0004-6256/135/1/338)
- Fukugita, M., Ichikawa, T., Gunn, J. E., et al. 1996, *AJ*, 111, 1748, doi: [10.1086/117915](https://doi.org/10.1086/117915)
- Gardner, E., & Done, C. 2017, *Monthly Notices of the Royal Astronomical Society*, 470, 3591, doi: [10.1093/mnras/stx946](https://doi.org/10.1093/mnras/stx946)
- Gaskell, C. M. 2004, *ApJ*, 612, L21, doi: [10.1086/424565](https://doi.org/10.1086/424565)
- Giustini, M., & Proga, D. 2019, *A&A*, 630, A94, doi: [10.1051/0004-6361/201833810](https://doi.org/10.1051/0004-6361/201833810)
- Goodman, J., & Weare, J. 2010, *CAMCoS*, 5, 65, doi: [10.2140/camcos.2010.5.65](https://doi.org/10.2140/camcos.2010.5.65)
- Graham, M. J., Djorgovski, S. G., Drake, A. J., et al. 2014, *Monthly Notices of the Royal Astronomical Society*, 439, 703, doi: [10.1093/mnras/stt2499](https://doi.org/10.1093/mnras/stt2499)
- Graham, M. J., Djorgovski, S. G., Stern, D., et al. 2015, *MNRAS*, 453, 1562, doi: [10.1093/mnras/stv1726](https://doi.org/10.1093/mnras/stv1726)
- Harris, C. R., Millman, K. J., van der Walt, S. J., et al. 2020, *Nature*, 585, 357, doi: [10.1038/s41586-020-2649-2](https://doi.org/10.1038/s41586-020-2649-2)
- Hobbs, G. 2013, *Class. Quantum Grav.*, 30, 224007, doi: [10.1088/0264-9381/30/22/224007](https://doi.org/10.1088/0264-9381/30/22/224007)
- Hu, Z., & Tak, H. 2020, *AJ*, 160, 265, doi: [10.3847/1538-3881/abc1e2](https://doi.org/10.3847/1538-3881/abc1e2)
- Hunter, J. D. 2007, *Comput. Sci. Eng.*, 9, 90, doi: [10.1109/MCSE.2007.55](https://doi.org/10.1109/MCSE.2007.55)
- Ingram, A., Done, C., & Fragile, P. C. 2009, *Monthly Notices of the Royal Astronomical Society: Letters*, 397, L101, doi: [10.1111/j.1745-3933.2009.00693.x](https://doi.org/10.1111/j.1745-3933.2009.00693.x)
- Ivezić, Ž., Smith, J. A., Miknaitis, G., et al. 2007, *The Astronomical Journal*, 134, 973, doi: [10.1086/519976](https://doi.org/10.1086/519976)
- Ivezić, Ž., Kahn, S. M., Tyson, J. A., et al. 2019, *ApJ*, 873, 111, doi: [10.3847/1538-4357/ab042c](https://doi.org/10.3847/1538-4357/ab042c)
- Jones, R. H., & Ackerson, L. M. 1990, *Biometrika*, 77, 721, doi: [10.1093/biomet/77.4.721](https://doi.org/10.1093/biomet/77.4.721)
- Kaczmarczik, M. C., Richards, G. T., Mehta, S. S., & Schlegel, D. J. 2009, *AJ*, 138, 19, doi: [10.1088/0004-6256/138/1/19](https://doi.org/10.1088/0004-6256/138/1/19)
- Kasliwal, V. P., Vogeley, M. S., & Richards, G. T. 2015, *Mon Not R Astron Soc*, 451, 4328, doi: [10.1093/mnras/stv1230](https://doi.org/10.1093/mnras/stv1230)
- . 2017, *Mon Not R Astron Soc*, 470, 3027, doi: [10.1093/mnras/stx1420](https://doi.org/10.1093/mnras/stx1420)
- Kelly, B. C., Bechtold, J., & Siemiginowska, A. 2009, *ApJ*, 698, 895, doi: [10.1088/0004-637X/698/1/895](https://doi.org/10.1088/0004-637X/698/1/895)
- Kelly, B. C., Becker, A. C., Sobolewska, M., Siemiginowska, A., & Uttley, P. 2014, *Astrophysical Journal*, 788, doi: [10.1088/0004-637X/788/1/33](https://doi.org/10.1088/0004-637X/788/1/33)
- Kozłowski, S. 2017, *A&A*, 597, 128, doi: [10.1051/0004-6361/201629890](https://doi.org/10.1051/0004-6361/201629890)
- . 2021, *AcA*, 71, 103, doi: [10.32023/0001-5237/71.2.2](https://doi.org/10.32023/0001-5237/71.2.2)

- Kubota, A., & Done, C. 2018, *Monthly Notices of the Royal Astronomical Society*, 480, 1247, doi: [10.1093/mnras/sty1890](https://doi.org/10.1093/mnras/sty1890)
- Leighly, K. M. 2004, *ApJ*, 611, 125, doi: [10.1086/422089](https://doi.org/10.1086/422089)
- Li, S.-L., & Cao, X. 2008, *Monthly Notices RAS Letters*, 387, L41, doi: [10.1111/j.1745-3933.2008.00480.x](https://doi.org/10.1111/j.1745-3933.2008.00480.x)
- Liu, F. T., Ting, K. M., & Zhou, Z.-H. 2008, in 2008 Eighth IEEE International Conference on Data Mining (Pisa, Italy: IEEE), 413–422, doi: [10.1109/ICDM.2008.17](https://doi.org/10.1109/ICDM.2008.17)
- Liu, T., Gezari, S., Burgett, W., et al. 2016, *ApJ*, 833, 6, doi: [10.3847/0004-637X/833/1/6](https://doi.org/10.3847/0004-637X/833/1/6)
- Luo, B., Brandt, W. N., Hall, P. B., et al. 2015, *The Astrophysical Journal*, 805, 122, doi: [10.1088/0004-637X/805/2/122](https://doi.org/10.1088/0004-637X/805/2/122)
- Lyke, B. W., Higley, A. N., McLane, J. N., et al. 2020, arXiv:2007.09001 [astro-ph]. <https://arxiv.org/abs/2007.09001>
- MacLeod, C. L., Ivezić, Ž., Kochanek, C. S., et al. 2010, *ApJ*, 721, 1014, doi: [10.1088/0004-637X/721/2/1014](https://doi.org/10.1088/0004-637X/721/2/1014)
- MacLeod, C. L., Ivezić, Ž., Sesar, B., et al. 2012, *The Astrophysical Journal*, 753, 106, doi: [10.1088/0004-637X/753/2/106](https://doi.org/10.1088/0004-637X/753/2/106)
- Matthews, T. A., & Sandage, A. R. 1963, *ApJ*, 138, 30, doi: [10.1086/147615](https://doi.org/10.1086/147615)
- McCaffrey, T. V., & Richards, G. T. 2021, doi: [10.17918/CIVdistance](https://doi.org/10.17918/CIVdistance)
- McKinney, W. 2010, in Python in Science Conference, Austin, Texas, 56–61, doi: [10.25080/Majora-92bf1922-00a](https://doi.org/10.25080/Majora-92bf1922-00a)
- McLaughlin, M. A. 2013, *Class. Quantum Grav.*, 30, 224008, doi: [10.1088/0264-9381/30/22/224008](https://doi.org/10.1088/0264-9381/30/22/224008)
- Moreno, J., Vogeley, M. S., Richards, G. T., & Yu, W. 2019, *PASP*, 131, 063001, doi: [10.1088/1538-3873/ab1597](https://doi.org/10.1088/1538-3873/ab1597)
- Mushotzky, R. F., Edelson, R., Baumgartner, W., & Gandhi, P. 2011, *ApJL*, 743, L12, doi: [10.1088/2041-8205/743/1/L12](https://doi.org/10.1088/2041-8205/743/1/L12)
- Novikov, I. D., & Thorne, K. S. 1973, in *Black Holes (Les Astres Occlus)*, 343–450
- Padmanabhan, N., Schlegel, D. J., Finkbeiner, D. P., et al. 2008, *The Astrophysical Journal*, 674, 1217, doi: [10.1086/524677](https://doi.org/10.1086/524677)
- Pereyra, N. A., Vanden Berk, D. E., Turnshek, D. A., et al. 2006, *ApJ*, 642, 87, doi: [10.1086/500919](https://doi.org/10.1086/500919)
- Peterson, B. M., Ferrarese, L., Gilbert, K. M., et al. 2004, *ApJ*, 613, 682, doi: [10.1086/423269](https://doi.org/10.1086/423269)
- Rankine, A. L., Hewett, P. C., Banerji, M., & Richards, G. T. 2020, *MNRAS*, 492, 4553, doi: [10.1093/mnras/staa130](https://doi.org/10.1093/mnras/staa130)
- Richards, G. T., McCaffrey, T. V., Kimball, A., et al. 2021, *AJ*, 162, 270, doi: [10.3847/1538-3881/ac283b](https://doi.org/10.3847/1538-3881/ac283b)
- Richards, G. T., Weinstein, M. A., Schneider, D. P., et al. 2001, *AJ*, 122, 1151, doi: [10.1086/322132](https://doi.org/10.1086/322132)
- Richards, G. T., Strauss, M. A., Fan, X., et al. 2006, *AJ*, 131, 2766, doi: [10.1086/503559](https://doi.org/10.1086/503559)
- Rivera, A. B., Richards, G. T., Hewett, P. C., & Rankine, A. L. 2020, *ApJ*, 899, 96, doi: [10.3847/1538-4357/aba62c](https://doi.org/10.3847/1538-4357/aba62c)
- Rivera, A. B., Richards, G. T., Hewett, P. C., Rankine, A. L., & Gallagher, S. C. 2021, in *American Astronomical Society Meeting Abstracts*, Vol. 53, American Astronomical Society Meeting Abstracts, 238.03D
- Roux, A. 2002, PhD thesis, University of Pretoria, Pretoria
- Róžańska, A., & Czerny, B. 2000, *A&A*, 360, 1170. <https://arxiv.org/abs/astro-ph/0004158>
- Rybicki, G. B., & Lightman, A. P. 1986, *Radiative Processes in Astrophysics*
- Sako, M., Bassett, B., Becker, A., et al. 2008, *The Astronomical Journal*, 135, 348, doi: [10.1088/0004-6256/135/1/348](https://doi.org/10.1088/0004-6256/135/1/348)
- Schneider, D. P., Gunn, J. E., & Hoessel, J. G. 1983, *ApJ*, 264, 337, doi: [10.1086/160602](https://doi.org/10.1086/160602)
- Sergeev, S. G., Doroshenko, V. T., Golubinskiy, Y. V., Merkulova, N. I., & Sergeeva, E. A. 2005, *ApJ*, 622, 129, doi: [10.1086/427820](https://doi.org/10.1086/427820)
- Sesar, B., Ivezić, Z., Lupton, R. H., et al. 2007, *The Astronomical Journal*, 134, 2236, doi: [10.1086/521819](https://doi.org/10.1086/521819)
- Shakura, N. I., & Sunyaev, R. A. 1973, *Astronomy and Astrophysics*, 24, 337
- Shemmer, O., & Lieber, S. 2015, *ApJ*, 805, 124, doi: [10.1088/0004-637X/805/2/124](https://doi.org/10.1088/0004-637X/805/2/124)
- Shen, Y., & Ho, L. C. 2014, *Nature*, 513, 210, doi: [10.1038/nature13712](https://doi.org/10.1038/nature13712)
- Shen, Y., Richards, G. T., Strauss, M. A., et al. 2011, *The Astrophysical Journal Supplement Series*, 194, 45, doi: [10.1088/0067-0049/194/2/45](https://doi.org/10.1088/0067-0049/194/2/45)
- Simm, T., Salvato, M., Saglia, R., et al. 2016, *A&A*, 585, A129, doi: [10.1051/0004-6361/201527353](https://doi.org/10.1051/0004-6361/201527353)
- Smith, K. L., Mushotzky, R. F., Boyd, P. T., et al. 2018, *ApJ*, 857, 141, doi: [10.3847/1538-4357/aab88d](https://doi.org/10.3847/1538-4357/aab88d)
- Sobolewska, M. A., Siemiginowska, A., & Życki, P. T. 2004, *ApJ*, 608, 80, doi: [10.1086/392529](https://doi.org/10.1086/392529)
- Starkey, D., Horne, K., Fausnaugh, M. M., et al. 2017, *ApJ*, 835, 65, doi: [10.3847/1538-4357/835/1/65](https://doi.org/10.3847/1538-4357/835/1/65)
- Stone, Z., Shen, Y., Burke, C. J., et al. 2022, arXiv e-prints, arXiv:2201.02762. <https://arxiv.org/abs/2201.02762>
- The Astropy Collaboration, A., Robitaille, T. P., Tollerud, E. J., et al. 2013, *Astronomy & Astrophysics*, Volume 558, id.A33, 9 pp., 558, doi: [10.1051/0004-6361/201322068](https://doi.org/10.1051/0004-6361/201322068)

- Uttley, P., & McHardy, I. M. 2001, *Monthly Notices of the Royal Astronomical Society*, 323, L26, doi: [10.1046/j.1365-8711.2001.04496.x](https://doi.org/10.1046/j.1365-8711.2001.04496.x)
- Vanden Berk, D. E., Wilhite, B. C., Kron, R. G., et al. 2004, *ApJ*, 601, 692, doi: [10.1086/380563](https://doi.org/10.1086/380563)
- Vio, R., & Andreani, P. 2018, arXiv e-prints, arXiv:1812.03995. <https://arxiv.org/abs/1812.03995>
- Virtanen, P., Gommers, R., Oliphant, T. E., et al. 2020, *Nat Methods*, 17, 261, doi: [10.1038/s41592-019-0686-2](https://doi.org/10.1038/s41592-019-0686-2)
- Wanders, I., Peterson, B. M., Alloin, D., et al. 1997, *ApJS*, 113, 69, doi: [10.1086/313054](https://doi.org/10.1086/313054)
- Wilhite, B. C., Brunner, R. J., Grier, C. J., Schneider, D. P., & Vanden Berk, D. E. 2007, *Monthly Notices of the Royal Astronomical Society*, 383, 1232, doi: [10.1111/j.1365-2966.2007.12655.x](https://doi.org/10.1111/j.1365-2966.2007.12655.x)
- Wilhite, B. C., Vanden Berk, D. E., Kron, R. G., et al. 2005, *ApJ*, 633, 638, doi: [10.1086/430821](https://doi.org/10.1086/430821)
- Wold, M., Brotherton, M. S., & Shang, Z. 2007, *MNRAS*, 375, 989, doi: [10.1111/j.1365-2966.2006.11364.x](https://doi.org/10.1111/j.1365-2966.2006.11364.x)
- York, D. G., Adelman, J., Anderson, J. E., et al. 2000, *AJ*, 120, 1579, doi: [10.1086/301513](https://doi.org/10.1086/301513)
- Yu, W., & Richards, G. T. 2022, EzTao: Easier CARMA Modeling. <http://ascl.net/2201.001>
- Zu, Y., Kochanek, C. S., Kozłowski, S., & Udalski, A. 2013, *The Astrophysical Journal*, 765, 106, doi: [10.1088/0004-637X/765/2/106](https://doi.org/10.1088/0004-637X/765/2/106)
- Zuo, W., Wu, X.-B., Liu, Y.-Q., & Jiao, C.-L. 2012, *ApJ*, 758, 104, doi: [10.1088/0004-637X/758/2/104](https://doi.org/10.1088/0004-637X/758/2/104)

APPENDIX

A. BIMODAL POSTERIOR DISTRIBUTIONS OF DHO PARAMETERS

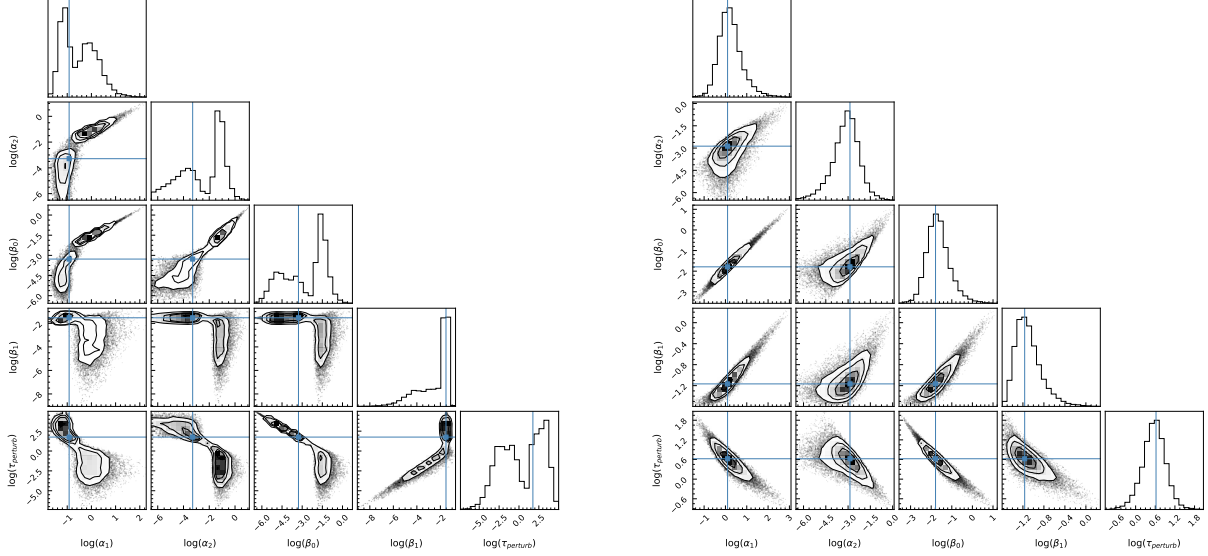


Figure 12. MCMC posterior distributions for DHO parameters: α_1 , α_2 , β_0 , β_1 , and τ_{perturb} . Shown are DHO fits for g -band light curves. *Left:* A selected example showing a bi-modal distribution; this example has a bi-modality index of 7.25. *Right:* A selected example showing a posterior distribution with a single mode; this example has a bi-modality index of 1.31.

By visually examining the posterior distribution of our MCMC samples, we found that some of them appear to be bi/multi-modal (see the left panel of Figure 12). We suspect this bi/multi-modality to have a mixture of different origins: intrinsic degeneracy (observed variability coming from different physical processes with comparable contributions), the poor sampling of our light curves, and strong emission lines landing in the range of the specific photometric bands. To automatically remove those fits from our analysis, we designed a bi-modality index S_{BM} ,

$$S_{\text{BM}} = \sigma_{\tau_{\text{perturb}}} + \sum_{y \in P} [\log(\gamma_y) + g(\tau_y) * \log(\tau_y/150)], \quad P = [\alpha_1, \alpha_2, \beta_0, \beta_1] \quad (\text{A1})$$

$$\gamma = (p_{75} - p_{25}) / (p_{99} - p_1) \quad (\text{A2})$$

$$g(\tau) = \frac{1}{1 + e^{-(\tau - 150)^{0.2}}} \quad (\text{A3})$$

where $\sigma_{\tau_{\text{perturb}}}$ is the “1-sigma” range of the posterior distribution of DHO’s τ_{perturb} in the log scale, τ is the auto-correlation time/step for the MCMC (see Foreman-Mackey et al. (2013)), and p_n is the n th percentile of the MCMC samples. Here, γ measures the tailness of the marginalized distribution. S_{BM} penalizes for large γ (small tails) and large τ (MCMC takes more steps to converge), both of which are indicators of potential bi/multi-modal distributions; at the same time, no incentives are given for small τ (implemented through $g(\tau)$ as an “activation function”). For a Gaussian distribution, γ has a nominal value of ≈ 0.3 . We also found that the MCMC chains for objects with single-mode posterior distributions (see the right panel of Figure 12) usually converge within 150 steps. $\sigma_{\tau_{\text{perturb}}}$ plays the role of identifying unconstrained posteriors. The distribution of $\sigma_{\tau_{\text{perturb}}}$ shows a natural break at 1.4, which is reasonable given that the cadence of our light curves is only sensible on timescales from 1 day to 2000 days—covering approximately 3 dex. That said, DHOs with $\sigma_{\tau_{\text{perturb}}}$ greater than 1.4 (a range of 2.8 dex) should be considered unconstrained. These realizations lead to a selection cut of $S_{\text{BM}} > 2.6$, where such DHO fits were not used for the analysis presented in Section 5. If the bi/multi-modal distribution is solely caused by emission lines contaminating the continuum variability, we should expect to see a higher percentage of objects being removed by our cut when the rest-frame effective wavelength is around an emission line or the Balmer Continuum (BC), which is also expected

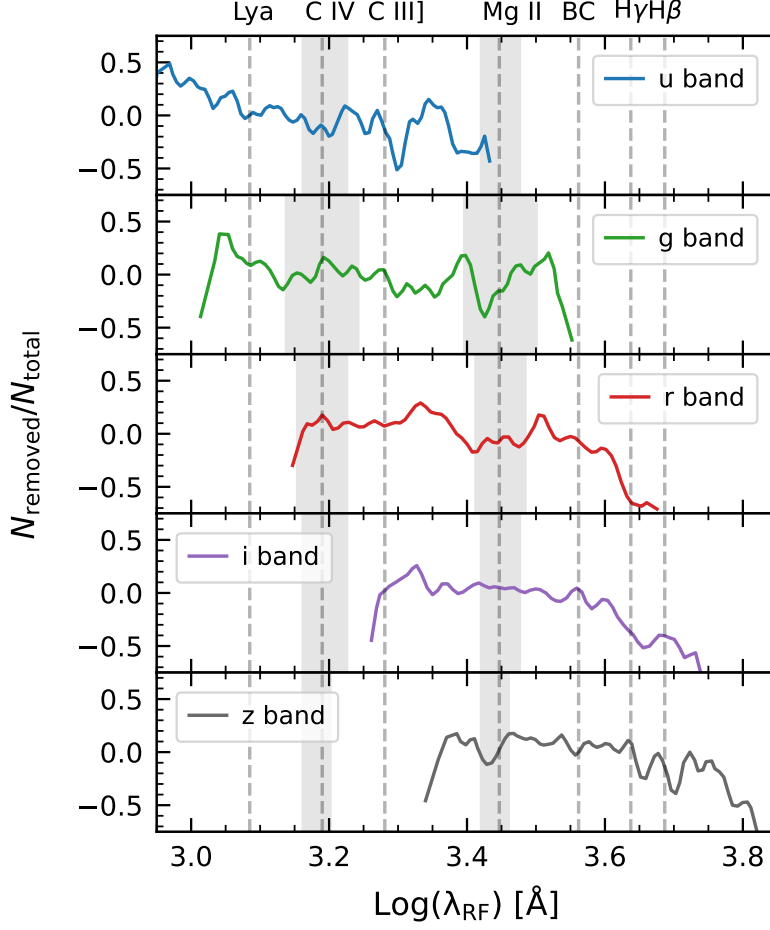


Figure 13. The percentage of DHO fits removed by a cut of $S_{\text{BM}} > 2.6$ as a function of the rest-frame effective wavelength of each photometric band. The shaded areas show the rest-frame coverage of the photometric bands centered at the C IV and Mg II emission lines. Some local peaks can be spotted at the wavelengths of emission lines (or within the shaded regions), e.g., at the C IV line for g and r bands, and at the Mg II line for r and z bands.

to be external to the disk. We investigated this expected effect and show the result in Figure 13. From Figure 13, we can see that in each band there are peaks occurring around the wavelengths of selected emission lines (or BC). Although not every emission line in every band has a matching local peak and the peaks are not as prominent, this is still a supportive evidence for our speculation that emission lines might contribute to the bi/multi-modal posterior distribution shown in Figure 12, at least partially. Emission line variability being a likely source of contamination for our analysis would be a good indicator of the promise of photometric reverberation mapping with the upcoming Rubin C. Observatory Legacy Survey of Space and Time (Chelouche & Daniel 2012; Chelouche et al. 2014; Ivezić et al. 2019).

B. SCALING OF σ_ϵ WITH REDSHIFT

According to Equation 8,

$$\sigma_{\text{DHO}}^2 = \frac{\beta_1^2 \alpha_2 + \beta_0^2}{2\alpha_1 \alpha_2} = \sigma_\epsilon^2 \left(\frac{\omega_0^2 \tau_{\text{perturb}}^2 + 1}{2\xi \omega_0^3} \right). \quad (\text{B4})$$

where $\omega_0 \propto T^{-1}$, $\tau_{\text{perturb}} \propto T$ (T is a timescale), and ξ is unitless. Since variability amplitude (σ_{DHO}) does not scale with redshift (z), we have,

$$\beta_0^2 = \sigma_\epsilon^2 = \sigma_{\text{DHO}}^2 \left(\frac{2\xi \omega_0^3}{\tau_{\text{perturb}}^2 \omega_0^2 + 1} \right) \propto T^{-3} \propto (1+z)^3 \quad (\text{B5})$$

which gives us $\beta_0 \propto (1+z)^{3/2}$.

C. OVERDAMPED DHO VS. DRW

The overdamped DHO model is similar to a DRW, but is more flexible. It would be interesting to compare the variability information extracted by the two models side by side using a same dataset. DRW can be generally characterized by an asymptotic amplitude (σ_{DRW}) and a long-term decay timescale (τ_{DRW}). The features extracted by DHO that are comparable to those two DRW parameters are σ_{DHO} and τ_{decay} . We fitted both models to the g -band light curves of our quasars. We compared σ_{DHO} with σ_{DRW} , σ_ϵ (the β_0 coefficient in Equation 1 and Equation 2) of DHO with that of DRW, and τ_{decay} of DHO with τ_{DRW} ; the results are shown in the top left, top right, and bottom left panel of Figure 14, respectively. From those three comparisons, we only found a good one-to-one correlation between σ_{DHO} and σ_{DRW} . One would have expected τ_{decay} of DHO to correlate with τ_{DRW} , since both characterize how long it takes for the modeled system to forget about its past self, however, we did not see that. Instead, we found a strong correlation between the ratio of τ_{decay} to τ_{perturb} and τ_{DRW} (see the bottom right panel of Figure 14). The slight “overestimation” of $\tau_{\text{decay}}/\tau_{\text{perturb}}$ at large τ_{DRW} can be explained by the well known underestimation of τ_{DRW} when the light curve span is shorter than 10 times the intrinsic τ_{DRW} (Kozłowski 2017), which is exactly what is being shown. We are not certain about the origin of this correlation, but if τ_{perturb} is physical then we suspect that the DRW model might be overlooking this information. More specifically, since DRW requires the perturbation process to be a white-noise with a flat power spectrum, then τ_{DRW} might be in units of τ_{perturb} because the DHO perturbation process only behaves like a white-noise at a timescale longer than τ_{perturb} (see the bottom left panel of Figure 3 for the power spectrum density of the DHO perturbation process). In addition, studies utilizing the power spectrum density technique have also suggested a potential second short-term characteristic timescale (relative to the known long-term decorrelation timescale) in AGN light curves, where the reported short-term timescales are comparable to the τ_{perturb} revealed in this work (Zu et al. 2013; Stone et al. 2022). We stress that the correlation shown between $\tau_{\text{decay}}/\tau_{\text{perturb}}$ and τ_{DRW} does not necessarily invalidate a DRW (or DHO) description of AGN variability, but argues for more careful examinations of the timescales returned by such modeling.

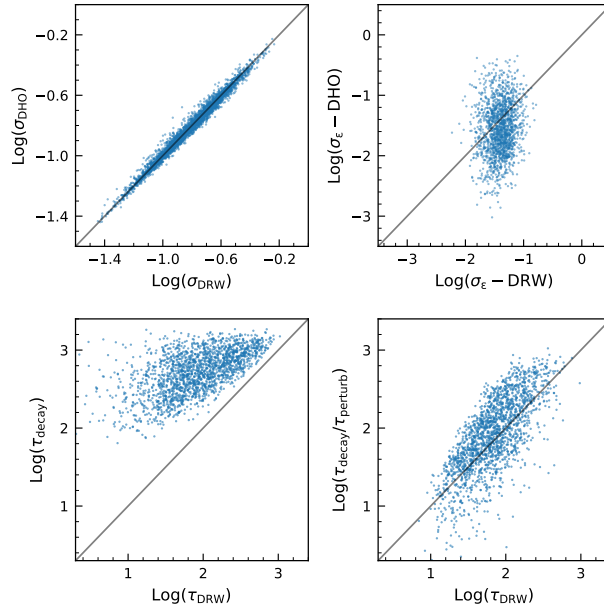


Figure 14. A comparison of similar variability signatures extracted by DHO and DRW. The black solid lines in each panel show the one-to-one correspondence. *Top left:* σ_{DHO} vs. σ_{DRW} , both characterize the asymptotic variability amplitude of the modeled system. *Top right:* Driving white noise amplitude (σ_ϵ) of DHO and of DRW. *Bottom left:* τ_{decay} of DHO vs. τ_{DRW} , both report the e-folding decay timescale of its auto-correlation function. *Bottom right:* $\tau_{\text{decay}}/\tau_{\text{perturb}}$ of DHO vs. τ_{DRW} .